Journal of
Intelligent Material
Systems and Structures

SI-ICAST2025

Journal of Intelligent Material Systems and Structures
1–27

DOI: 10.1177/1045389X261461627
journals.sagepub.com/home/jim
Sage

Investigation of arbitrarily-shaped encapsulated bubbles for attenuation low-frequency underwater sound

Ana Carolina Azevedo Vasconcelos[1] and **Jovana Jovanova**[1]

Abstract

The increasing installation of large offshore monopiles for wind turbine foundations generates harmful underwater noise during pile driving, particularly at low frequencies. Existing noise mitigation systems target noise around 1000 Hz, however, their performance reduces for lower frequency noise expected for the upcoming monopiles. To address this, this paper develops and investigates a new noise mitigation system – a metamaterial-based curtain, or meta-curtain-using metamaterials and smart materials to filter sound waves generated during the pile installation, focusing mainly on the primary noise source – from pile to water. The meta-curtain is developed via a design methodology that covers the understanding of bubble fundaments, the attenuation performance in the pile-water system, and the structural integrity and deployment mechanism of the curtain frame. This paper focuses mainly on the steps related to the acoustic of the new bubble designs and their attenuation performance. Future work explores the structural performance of the meta-curtain. This work opens the door to the investigation of new designs that can potentially reduce the propagation of low-frequency waves from monopile installations.

Keywords

bubbly membranes, vibration attenuation, monopile installation

Introduction

The increasing installation of offshore wind farms across Europe is boosted to meeting the 42.5% renewable energy target by 2030 (WindEurope, 2023). To support such wind farms, monopiles are typically used as foundations due to their cost-effectiveness and ease of installation. Current monopile sizes range from 4 to 8 m and 25 to 40 m in diameter and length, respectively (Ma and Yang, 2023; Murphy et al., 2018; Wang et al., 2020), however, future wind farms are expected to require even larger monopiles (WindEurope, 2022). The installation process involves driving the monopile into the seabed through impact hammer blows, which can provide energy ranging from 150 to 6600 kJ (IQIP, 2024). The high impact hammer blow induces longitudinal wave propagation, leading to pile resonance that radially excites the pile wall. This radial motion interacts with the surrounding water, emitting noise waves that can travel long distances in marine environment, causing potential risks to marine life, such as hearing loss and even death (Dahl et al., 2015; Reinhall and Dahl, 2011; Solé et al., 2017).

To mitigate the negative effects of environmental noise, several noise mitigation systems have been developed. From those, the most commonly used are the air bubble curtains and the hydro sound dampers. Air bubble curtains consist of air bubbles released from the seabed, rising to the seasurface. The bubbles create an air layer, which changes drastically the impedance in the water environment.

The installation of the upcoming offshore monopiles requires noise mitigation systems (NMSs) able to reduce low-frequency noise, which has shown to be harmful to marine life. The traditional NMSs have demonstrated significant reduction levels in frequency ranges varying from 500 Hz to 5 kHz. However, when it comes to frequencies below 500 Hz, the efficiency of such systems drops significantly. For instance, air bubble curtains, which are the most common mitigation

[1]Faculty of Mechanical Engineering, Delft University of Technology, The Netherlands

Corresponding author:
Ana Carolina Azevedo Vasconcelos, Faculty of Mechanical Engineering, Delft University of Technology, Mekelweg 2, Delft 2628 CD, The Netherlands.
Email: carol.azevedo856@gmail.com

Data Availability Statement included at the end of the article

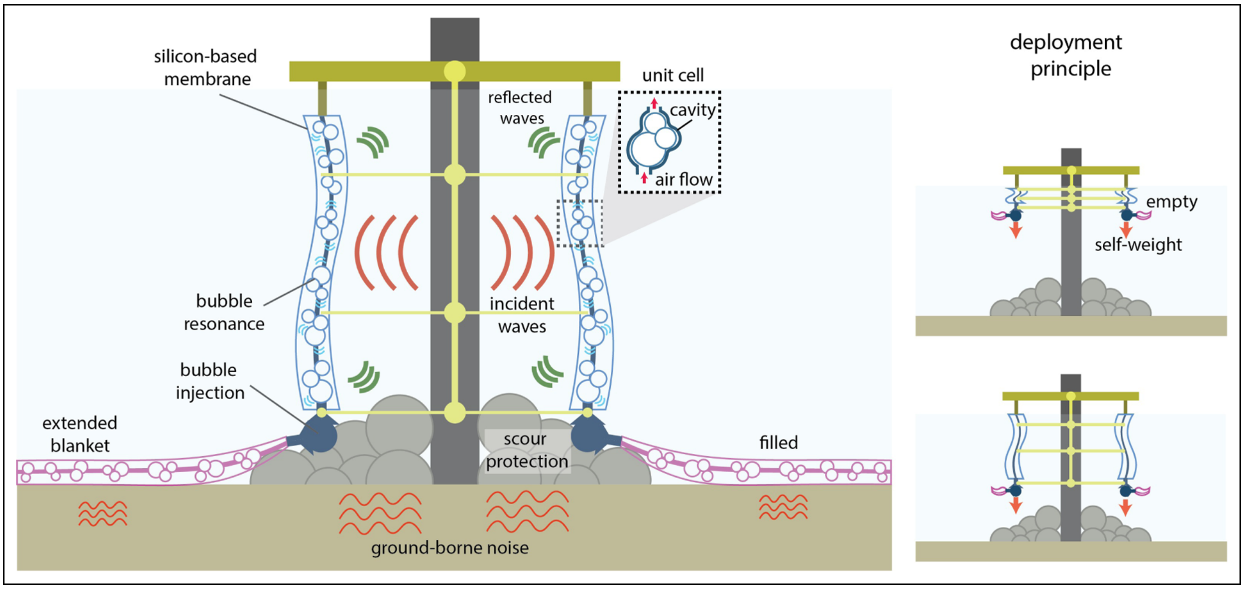

Figure 1. Schematic of the meta-curtain with its attenuation mechanism and potential deployment principle.

system, require the generation of large air bubbles to mitigate low-frequency noise, demanding high energy supply. In addition to that, large bubbles are unstable and can split into small parts, reducing their efficiency in attenuating low-frequency noise. Solutions for low-frequency noise emission have also focused on combining several NMSs, such as double big bubble curtains and IHC-NMS combined with big bubble curtains. Despite such systems have shown significant noise attenuation, their installation and operation are very costly. Besides that, the current NMSs have mainly focused on mitigating the primary noise source, that is, the sound waves transmitted directly from the pile to the water, while the noise transmitted from the secondary noise path (elastic wave induced by the monopile propagates from the soil to water) is less explored, specially due to the complexity in soil dynamics. Therefore, exploring new NMS designs targeting the new critical frequency noise is highly necessary to maintain a safe environment for marine life and keep offshore wind-farm installation in place so that the energy transition can be achieved.

This paper aims to develop and investigate a new NMS consisting of a bubble curtain that can reduce low-frequency underwater noise. The uniqueness of this design relies on the use of metamaterials principle, where their microstructure is defined to achieve unique properties not common in nature materials, embedded in flexible membranes to reduce the underwater noise, while investigating the flexibility-rigidity balance required for the deployment process. To achieve these goals, this paper presents a design methodology of encapsulated air bubbles, where the bubble fundamentals are explored in an acoustic model and the attenuation mechanism is evaluated in a vibroacoustic numerical model containing the pile-water-soil system. The methodology also suggests a structural model to consider the deployment mechanism and structural integrity of the bubble curtain frame, although a dedicated work will explore this investigation. The methodology ends by prototyping encapsulated bubbles and validating their functionality in a small-scale test setup. The proposed methodology shares methodological parallels with established approaches in computational mechanics. The extraction of effective acoustic properties from the bubbly medium is analogous to homogenization techniques in porous media, where macroscopic transport properties are derived from microstructural analysis. The multi-scale framework-from unit-cell acoustics to effective medium representation to system-level vibroacoustic modeling – follows a hierarchical paradigm common in damage mechanics and composite material design.

The novel metamaterial-based curtain formed by two main attenuation components – one is designed to filter the primary noise source while the second filters the noise coming via pile-soil-water path. The first component is designed to prevent the propagation of low-frequency sound waves induced by the monopile vibration. It includes a silicone-based/textile membrane with cavities, or unit cells, filled with air bubbles injected from below (see blue membrane in Figure 1). These cavities are arranged in a specific pattern to meet environmental conditions and targeted noise reduction levels, particularly in the low-frequency range. Different cavity geometries can be designed to target distinct frequency ranges, allowing increased noise attenuation performance. The design's flexibility enables quick deployment and minimizes damage risk during contact with the monopile. Some preliminary deployment aspects

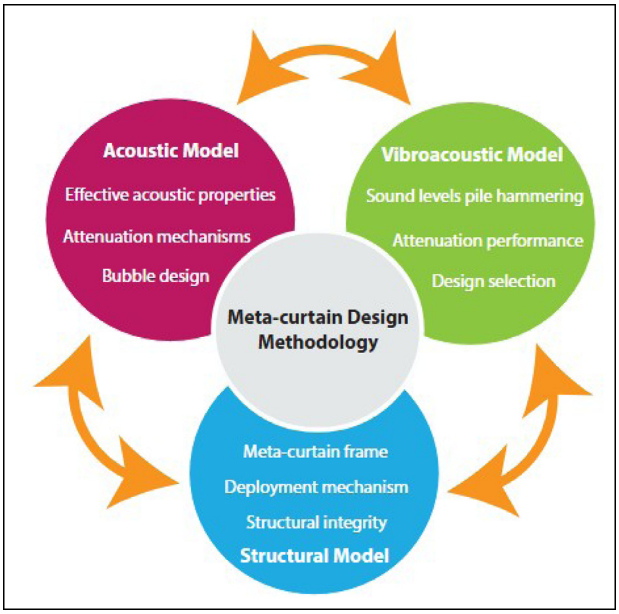

Figure 2. Three-step design methodology of the meta-curtain for underwater noise mitigation during pile hammering.

will be addressed to move toward a design with proper noise mitigation-deployment balance. The second component will improve the secondary noise path attenuation (purple membrane in Figure 1). Addressing the secondary noise path is beyond the scope of this study but is recommended for future investigation to achieve a more comprehensive design.

Design methodology of meta-curtain

The design of the meta-curtain follows a three-step methodology, as depicted in Figure 2. In the first step, the acoustic properties of air bubbles – varying in size, shape, and membrane thickness – are investigated through theoretical and numerical models to understand their attenuation mechanisms, extract effective acoustic properties, and evaluate attenuation performance. Numerical results are verified with established theoretical models. Once promising bubble designs are identified, prototypes are fabricated and tested in a small-scale tank.

These effective acoustic properties then inform the second step, where the bubble's ability to attenuate noise from monopile installation is assessed. Numerical vibroacoustic models are developed to predict the underwater sound levels during impact-driven activity without and with the bubble's influence.

While the first two steps focus on acoustic performance, the final step addresses the physical structure that holds the bubbles in place underwater and its deployment mechanism. A structural model is proposed to ensure integrity during deployment and prevent buoyancy issues caused by the bubbles – aiming to balance rigidity and flexibility. A prototype is built and its deployment is tested in an underwater environment.

This paper primarily focuses on the steps related to the studies of an acoustic model and a vibroacoustic model, including the theoretical modeling of free and encapsulated bubbles, and development of numerical models for the bubble dynamics and their interaction with a pile-water-soil system. An experimental setup is also proposed to evaluate the bubble performance in a small-scale tank. The step related to the structural model exploring deployment mechanisms and its interaction with the offshore environment is investigated in a future work.

Acoustic properties of air bubbles

Air bubbles have been used to attenuate underwater noise based on two mechanisms: resonance phenomena of the bubbles and acoustic impedance mismatching between the bubbly water and bubble-free water. This section discusses how such mechanisms rise from freely-rising bubbles and encapsulated bubbles.

Theoretical approach of free air bubbles

The model developed by Commander and Prosperetti (1989) calculates the complex acoustic velocity in a bubbly fluid, where fluid's viscosity, heat conduction, acoustic radiation and dispersion effects are considered. The complex acoustic velocity c_m and damping coefficient b are

$$\frac{c_l^2}{c_m^2} = 1 + \frac{4\pi c_l^2 nr}{\omega_b^2 - \omega^2 + 2ib\omega}, \tag{1}$$

and

$$b = \frac{2\mu}{\rho_l r^2} + \frac{p_b}{2\rho_l r^2 \omega}\mathrm{Im}\Phi + \frac{\omega^2 r}{2c_l}, \tag{2}$$

where i is the imaginary unit; n is the number of bubbles per unit volume; c_l, ρ_l, and μ are the acoustic speed, density, and viscosity of the host liquid; and ω is the angular excitation frequency. The damping coefficient b comprises three terms related to the viscous damping, heat dissipation damping, and acoustic radiation damping, from left to right. The resonance of an air bubble ω_b is given by, in rad/s,

$$\omega_b^2 = \frac{p_b}{\rho_l r^2}\left(\mathrm{Re}[\Phi] - \frac{2\sigma}{rp_b}\right), \tag{3}$$

where p_b is the equilibrium pressure at the bubble's surface (given by $p_b = p_h + 2\sigma/r$, where p_h is the hydrostatic pressure in the liquid), r is the bubble radius, and σ is the surface tension of the liquid (Wang et al., 2022).

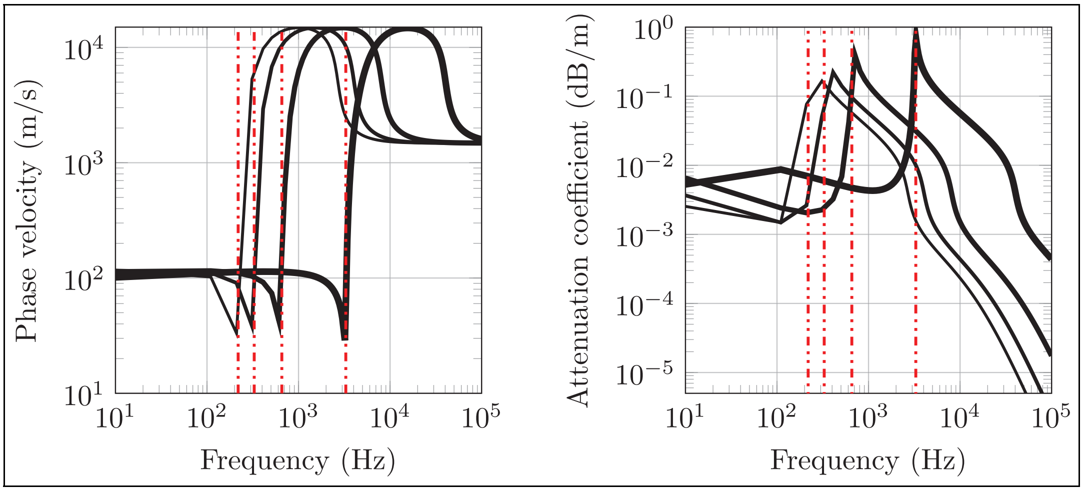

Figure 3. Effective wave speed and attenuation coefficient variation with respect to frequency. From thin to thick curves, the bubble radius are $r = 1.5$ cm, $r = 1$ cm, $r = 0.5$ cm, $r = 0.1$ cm, which gives a resonance frequency of 219, 328, 657, and 3285 Hz, respectively (indicated by red vertical lines). A volume fraction of 0.01 was used.

Φ is a complex function related to the dynamics of the bubble as it expands and contracts, which is given by

$$\Phi = \frac{3\gamma}{1 - 3i\chi(\gamma - 1)[(i/\chi)^{1/2}\coth(i/\chi)^{1/2} - 1]}, \quad (4)$$

where $\chi = D/(\omega r^2)$, being D and γ the thermal diffusivity and the specific heat capacity of the gas phase, respectively. In the further studies, we will assume $D = 18.46 \times 10^{-6}$ m^2/s and $\gamma =$ 1.4 (Beelen et al., 2025). Equation (3) can be simplified as

$$\omega_b^2 = \frac{1}{r^2}\frac{3\gamma p_b}{\rho_l} \quad (5)$$

which is known as Minnaert frequency ($f_M = 2\pi\omega_b$) and gives the pulsation mode of an air bubble.

Figure 3 shows the phase velocity and attenuation coefficient predicted by the Commander and Prosperetti model (Commander and Prosperetti, 1989). Bubble radius of 1.5, 1, 0.5, and 0.1 cm are investigated, from which resonance frequencies are 219, 328, 657, and 3285 Hz, respectively. Below the resonance, the bubbles behave similarly to an acoustically soft medium, which has a low effective bulk modulus. This creates a strong impedance mismatch with water, though with low absorption, since energy dissipation is not efficient due to low damping. Above the resonance, the bubbles oscillates out of phase with the pressure field, influencing thermal, viscous, and radiation damping, which leads to high energy dissipation. The impedance mismatch still holds at frequencies above resonance, since the bubbly medium becomes stiffer due to the increase of effective bulk modulus. The resonant effects decrease after a certain frequency.

Another important design variable considered when designing bubble curtains is the volume fraction (VF), which gives the ratio between the air volume occupied by the bubbles and the total volume of the curtain as follows

$$VF = \frac{NV_b}{V_t}, \quad (6)$$

where N is the number of encapsulated bubbles, V_b is the mean single bubble volume, and V_t is the total volume inside the frame where the bubbles are placed.

Figures 4 and 5 show the effect of volume fraction on the effective wave speed and attenuation coefficient for different bubble sizes interacting with sound waves of frequency $f = 100$ Hz and $f = 1000$ Hz, respectively. At 100 Hz (Figure 4), all bubble sizes operate in the sub-resonance regime (f $< f_M$), where the effective phase speed decreases and attenuation increases monotonically with volume fraction due to impedance mismatch. Notice that for small volume fractions, the phase velocity approaches the sound velocity in water, while for a medium with high volume fraction, the phase velocity considerably decreases. This condition only holds for waves of frequency below the resonance frequency of the bubble, since in Figure 5, the phase velocity behavior changes for waves of frequency higher than the resonance frequency of the bubble. At 1000 Hz (Figure 5), the behavior differs significantly across bubble sizes. For $r = 0.5$ cm, the Minnaert frequency ($f_M = 653$ Hz) is closest to the analysis frequency, causing a pronounced peak in phase velocity near resonance. For $r = 0.1$ cm, the resonance frequency ($f_M = 3265$ Hz) is well above 1000 Hz, so the medium remains in the sub-resonance regime. The

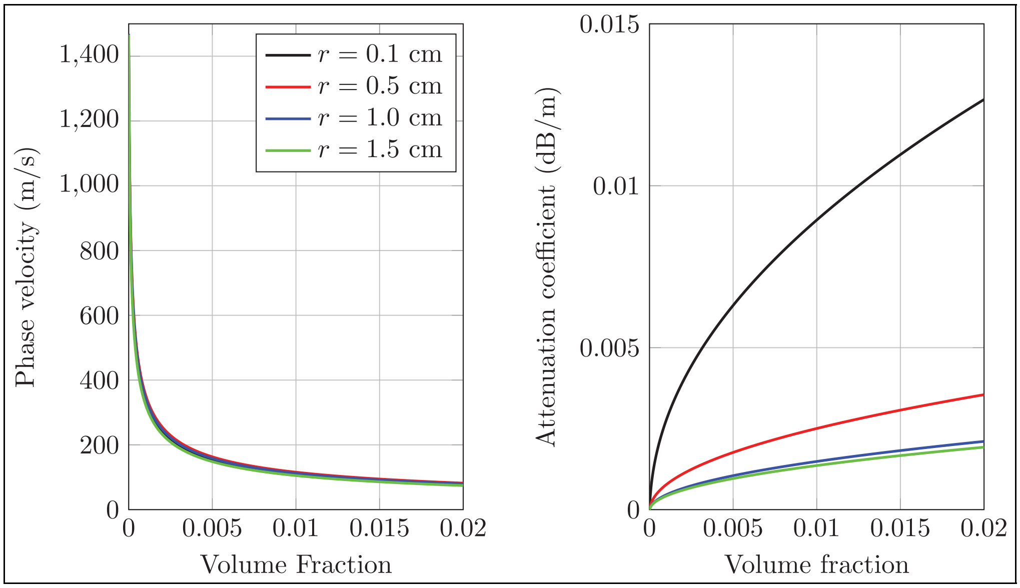

Figure 4. Effective wave speed and attenuation coefficient variation with respect to volume fraction. The bubble radius are $r = 1.5$ cm, $r = 1$ cm, $r = 0.5$ cm, $r = 0.1$ cm. A frequency of 100 Hz was used.

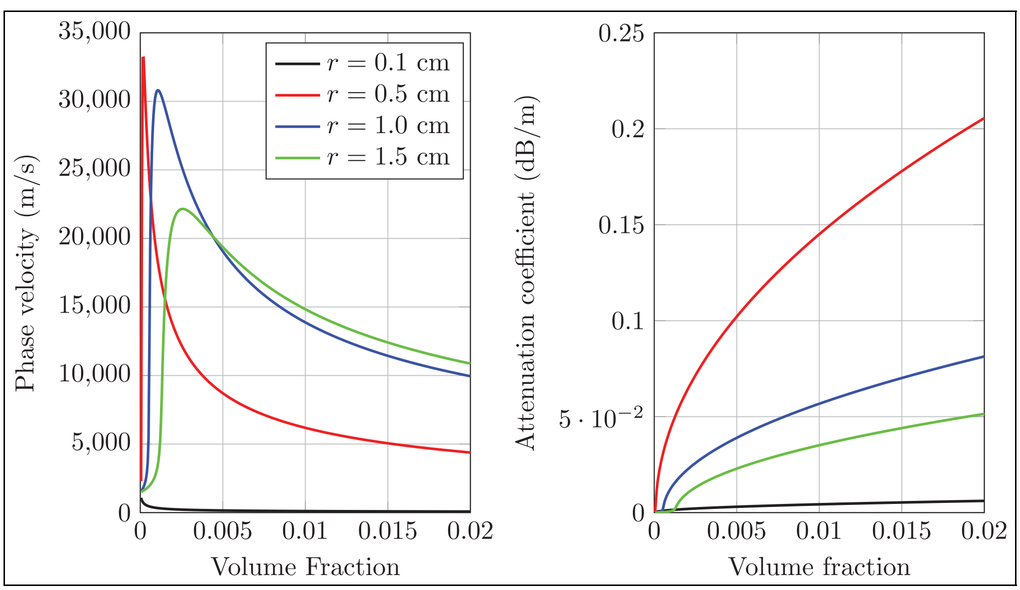

Figure 5. Effective wave speed and attenuation coefficient variation with respect to volume fraction. The bubble radius are $r = 1.5$ cm, $r = 1$ cm, $r = 0.5$ cm, $r = 0.1$ cm. A frequency of 1000 Hz was used.

markedly different trends in attenuation coefficient at 100 and 1000 Hz are thus explained by the relative position of the analysis frequency with respect to each bubble's resonance frequency.

Inducing low frequency resonance would require large free bubbles with radii in the order of centimeter. Bubbles of such size are usually unstable and could break up into smaller bubbles. To overcome this limitation, bubbles are encapsulated within a thin elastic shell made of some material. This offers the advantage of more control over the bubble volume and its resonance frequency. The material used to cover the bubbles should be elastic and thin enough to allow the bubble resonance and robust enough for deployment in the marine environment. In the next section, the theoretical approach for modeling encapsulated bubbles is presented.

Theoretical approach of encapsulated air bubbles

The acoustic behavior of bubbles coated with a solid elastic shell has been described by the theoretical model proposed by Church (1995). This model states that the wavenumber k_m, the bubble resonance ω_0, and the damping coefficients δ_i are given by:

$$k_m^2 = k^2 + \frac{4\pi\omega^2\rho_l}{\eta\rho_s}\int_0^\infty \frac{r_1 f(r_1)}{\omega_0^2 - \omega^2 + i(\delta_{v,s} + \delta_{v,l} + \delta_t + \delta_a)\omega} dr_1, \tag{7}$$

$$\omega_0^2 = \frac{1}{\rho_s r_1^2 \eta} \left(3\kappa P_0 - \frac{2\sigma_1}{r_1} - \frac{2\sigma_2 r_1^3}{r_2^4} + 4\frac{V_s G_s}{r_2^3}\left[1 + Z\left(1 + \frac{3r_1^3}{r_2^3}\right)\right]\right), \tag{8}$$

$$\delta_{v,s} = \frac{2V_s\mu_s}{r_2^3}\left(\rho_s r_1^2\right)^{-1}, \tag{9}$$

$$\delta_{v,l} = \frac{2\mu_l r_1^3}{r_2^3}\left(\rho_s r_1^2 \eta\right)^{-1}, \tag{10}$$

$$\delta_t = 2\mu_{th}\left(\rho_s r_1^2 \eta\right)^{-1}, \tag{11}$$

$$\delta_a = \frac{1}{2}\omega k r_2 [1 + (kr_2)^2]^{-1}, \tag{12}$$

where $k = \omega/c_l$ is the wavenumber for the medium, r_1 is the inner radius of an individual bubble, r_2 is the outer radius of the bubble with shell thickness r_s, $V_s = r_2^3 - r_1^3$, P_0 is the ambient pressure, ρ_s is the density of the shell material, and $f(r_1)$ is the bubble size distribution function. The remaining parameters of the shell material are its shear modulus G_s, viscosity μ_s, the interfacial tension of the shell/bubble boundary σ_1, and the interfacial tension at the shell/liquid boundary σ_2. Due to the presence of the encapsulating shell, the individual bubble resonance frequency and damping terms are different from the free bubble terms – the shell stiffness increases the individual bubble resonance frequency and the additional damping term $\delta_{v,s}$ is required to take into account viscous losses in the shell.

The additional terms η and Z are related to the properties at the shell/bubble and shell/liquid interface and are given by:

$$\eta = \left[1 + \left(\frac{\rho_l - \rho_s}{\rho_s}\right)\frac{r_1}{r_2}\right] \tag{13}$$

and

$$Z = \frac{1}{4G_s}\left[\frac{2\sigma_1}{r_1} + \frac{2\sigma_2}{r_2}\right]\frac{r_2^3}{V_s}. \tag{14}$$

The phase speed c_m and attenuation α (in Np/m) are computed from the dispersion relation using the following relations:

$$c_m = \frac{\omega}{\Re(k_m)} \tag{15}$$

and

$$\alpha = \Im(k_m). \tag{16}$$

To visualize the effective properties provided by the theoretical model of the encapsulated bubble, the interfacial tensions of the shell/bubble boundary and shell/liquid boundary, σ_1 and σ_2, need to be experimentally retrieved, which is outside of the scope of this project.

Numerical approach of effective acoustic parameters

The acoustic parameters of the free and encapsulated bubbles will be retrieved via two numerical models developed in the commercial software Comsol Multiphysics. The first model consists on an eigenfrequency study where the bubble natural frequencies are obtained. In the second model, the effective parameters of the bubbles, density, impedance and reflection and transmission coefficients, are obtained via a time-harmonic analysis. This model will be used to investigate the effect of the bubble resonance on the effective properties.

A 2D axisymmetric model of single free and encapsulated bubbles is used to extract their natural frequencies, as shown in Figure 6. In both models, the air bubble and water that surround the bubble are modeled as thermoviscous acoustics to consider the viscous and thermal losses. The thermophysical and acoustic properties of water at 20°C are density $\rho_l = 998$ kg/m^3, speed of sound $c_l = 1481$ m/s, dynamic viscosity $\mu_l = 1.002 \times 10^{-3}$ Pa·s, thermal conductivity $\kappa_l = 0.607$ W/(m·K), specific heat $C_{p,l} = 4182$ J/(kg·K), bulk viscosity $\mu_{B,l} = 2.4 \times 10^{-3}$ Pa·s. For air at 20°C, the properties are density $\rho_g = 1.225$ kg/m^3, speed of sound $c_g = 343$ m/s, dynamic viscosity $\mu_g = 1.81 \times 10^{-5}$ Pa·s, thermal conductivity $\kappa_g = 0.026$ W/(m·K), specific heat $C_{p,g} = 1005$ J/(kg·K), and ratio of specific heat $\gamma = 1.4$. The outer water layer is modeled as pressure acoustics, with its outer edge modeled as a spherical wave radiation to reduce the reflections on the model. The difference between the free and encapsulated models relies on the interface conditions. For free bubbles (Figure 6(a)), surface tension is assumed on the air-water interface, where a surface tension coefficient $\sigma = 0.0725$ N/m is assumed. For the encapsulated bubble model (Figure 6(b)), thermoviscous acoustic-structure interaction is assumed at the air-membrane interface and the membrane-water interface. Atmospheric pressure is assumed in all domains.

Effective acoustic properties of the meta-curtain

The retrieving method has been chosen to determine the effective acoustic properties of a bubbly domain

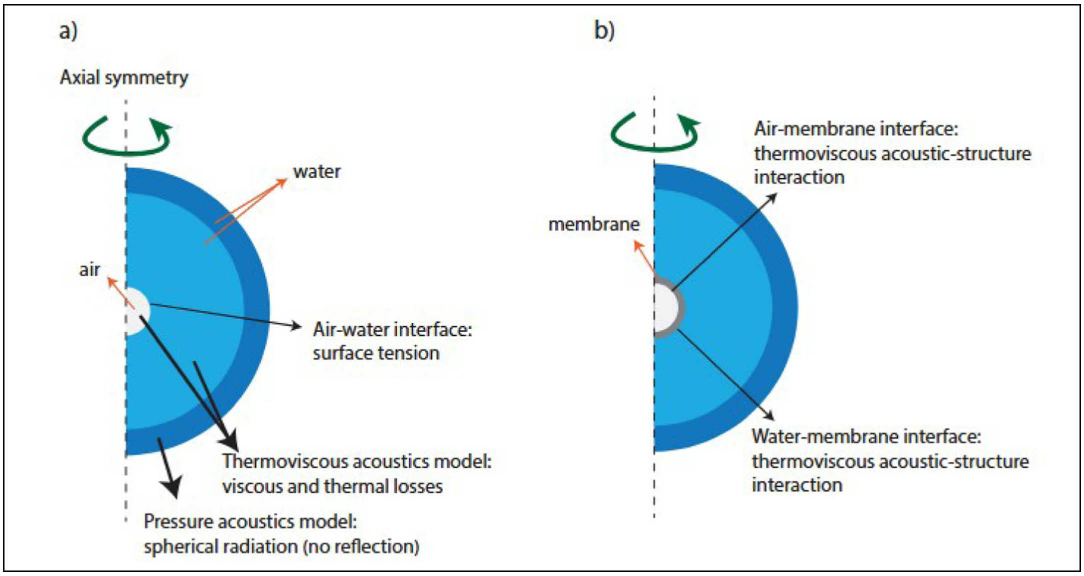

Figure 6. Numerical model to obtain the natural frequencies of (a) free bubbles and (b) encapsulated bubbles.

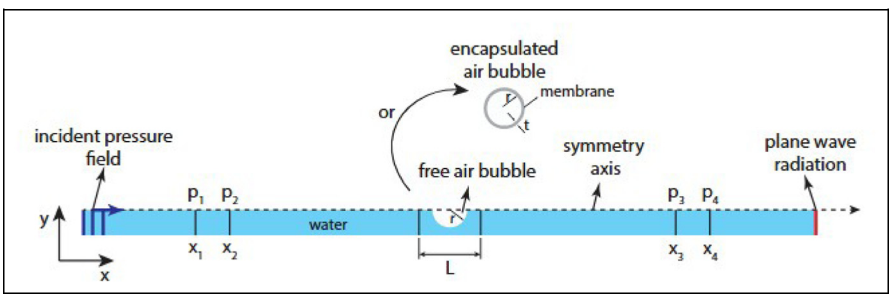

Figure 7. Numerical model to retrieve the effective acoustic properties of free and encapsulated air bubbles.

containing free or encapsulated bubbles (Henríquez et al., 2017). In this method, the reflection and transmission coefficients, as well as the effective acoustic properties (mass density and acoustic impedance), are obtained by evaluating the pressure field at specific positions of a symmetric waveguide containing a bubbly medium of size L, as shown in Figure 7– the size of the bubble medium is defined in terms of the desired volume fraction. An incident pressure field of amplitude is applied on the left boundary, while a plane wave radiation is assumed on the right boundary to reduce wave reflections.

The reflection and transmission coefficients are extracted through the relation between the incident and reflected waves and incident and transmitted waves, respectively. These coefficients are expressed as:

$$R = \frac{p_2 e^{-ikx_1} - p_1 e^{-ikx_2}}{p_1 e^{ikx_2} - p_2 e^{ikx_1}}, \tag{17}$$

$$T = \frac{p_3}{p_2} \frac{e^{-ikx_2} + Re^{ikx_2}}{e^{-ikx_3}} e^{-ikL}, \tag{18}$$

where p_1, p_2, and p_3 are the average total pressure measured at the edges located at positions x_1, x_2, and x_3, respectively. The effective wave number and acoustic impedance are calculated in terms of the reflection and transmission coefficients via the following expressions:

$$k_{\text{eff}} = \frac{1}{L}\cos^{-1}\left(\frac{1 + T^2 - R^2}{2T}\right), \tag{19}$$

$$Z_{\text{eff}} = Z_1 \frac{1 + R - T\cos(k_{\text{eff}}L)}{iT\sin(k_{\text{eff}}L)}. \tag{20}$$

From the wave number and acoustic impedance, the effective mass density, wave speed, and bulk modulus can be derived through $\rho_{\text{eff}} = Z_{\text{eff}}k_{\text{eff}}/\omega$, $c_{\text{eff}} = \omega/k_{\text{eff}}$, and $\kappa_{\text{eff}} = Z_{\text{eff}}\omega/k_{\text{eff}}$, respectively. Transmission loss (TL) is calculated as follows:

$$\text{TL} = 20\log_{10}\left(\frac{1}{\|T\|}\right). \tag{21}$$

Considering a free air bubble of radius $r = 1$ cm, the Minnaert frequency, according to equation (5), is given

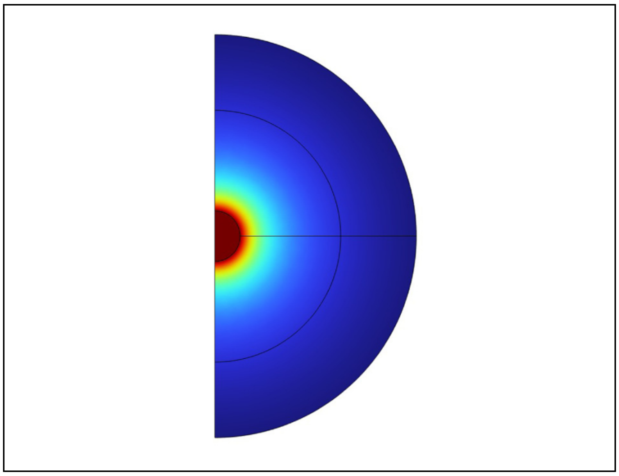

Figure 8. Pulsation mode of 1 cm radius free air bubble identified at frequency 327.24 Hz. The colormap indicates the total acoustic pressure variation, where changes from highest values (dark red) to lowest values (dark blue).

by f_M = 328 Hz. This agrees with the result presented in Figure 3. The eigenfrequency study performed in Comsol Multiphysics gives a pulsation mode of 327.24 Hz, which agrees with the resonance frequencies determined via the theoretical models, as shown in Figure 8.

The effective acoustic properties of the studied bubble can be obtained by evaluating the behavior of reflected and transmitted pressure fields inside a waveguide, as explained in Figure 7. Using the corresponding pressure fields in equations (17)–(20), the effective acoustic properties are obtained as shown in Figure 9. Notice that the transmission coefficient shifts from near one to almost zero at frequency f = 337 Hz, which is near the resonance frequency of the bubble estimated by the eigenfrequency analysis. Moreover, the sum of the reflection and transmission coefficients for each frequency step is approximately one (R + T = 1), indicating that the model respects the energy conservation. In this frequency, the reflection coefficient increases, indicating that the waves are reflected due to the bubble resonance. The difference in the resonance frequency can be attributed to the outer boundary condition, once in the eigenfrequency analysis a spherical wave radiation (no reflection) is assumed.

The effective mass density ρ_{eff} and effective phase velocity c_{eff} (Figure 9(b) and (c)) in the low-frequency regime approach the value of density and velocity in water. For frequencies near the resonance frequency of the bubble the effective properties shift toward lower values and suddenly increase, creating a system with a high contrast in impedance. After the resonance regime, the acoustic properties tend to restore the initial values. The reduction in acoustic properties near the resonance has also been demonstrated in the theoretical results, as shown in Figure 3.

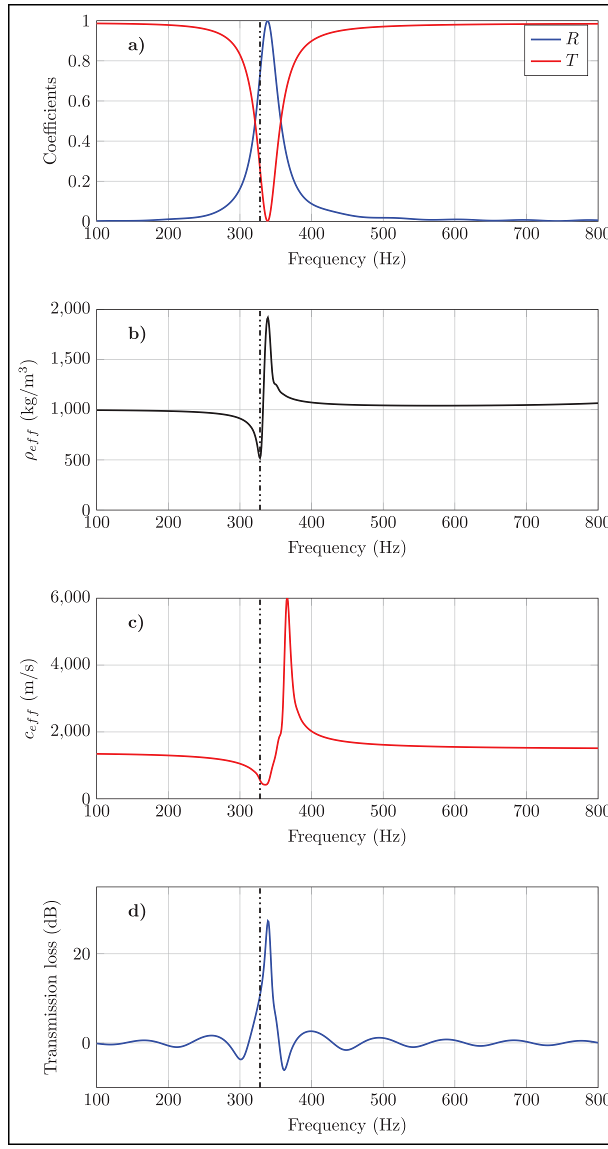

Figure 9. (a) Reflection and transmission coefficients obtained through equations (17) and (18), (b) Effective mass density, (c) effective phase velocity, and (d) transmission loss for a free bubble of radius r_b = 1 cm inside a water waveguide. The black vertical line indicate the resonance frequency predicted by the eigenfrequency analysis.

To investigate the attenuation performance of the bubble at frequencies near its resonance frequency, the transmission loss, calculated through equation (21), is obtained as shown in Figure 9(d). Notice that a peak in transmission loss is observed toward the resonance frequency of the bubble, which has also been confirmed by the decrease in the transmission coefficient indicated in Figure 9(a).

Considering an air bubble of radius r = 1 cm encapsulated by a silicone membrane of thickness r_s = 2 mm with material properties Young's modulus E_s = 0.069 MPa, density ρ_s = 1070 kg/m^3, and Poisson's ratio

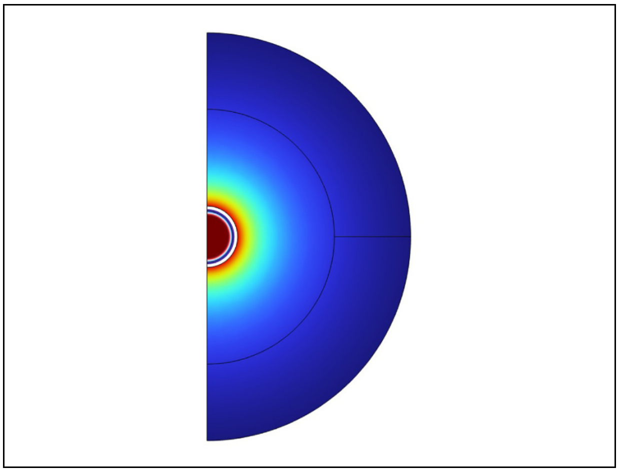

Figure 10. Pulsation mode identified at frequency 339.39 Hz of an 1 cm radius air bubble encapsulated with a silicone membrane of thickness $r_s = 2$ mm. The colormap indicates the total acoustic pressure variation for air bubble and water domains and displacement magnitude for the membrane.

$\nu_s = 0.4997$, the resonance frequency determined via numerical model is shown in Figure 10.

As expected, the resonance frequency increases slightly in comparison to the free bubble case due to the inclusion of the stiffness related to the silicone membrane. In terms of the effective acoustic properties of the encapsulated bubble, Figure 11 shows the reflection and transmission coefficients, as well as the effective mass density and phase velocity and transmission loss of the encapsulated bubble obtained via the retrieve method. Notice that the primary peak aligns with the eigenfrequency of 339.39 Hz (Figure 10), shifted upward from the free bubble Minnaert frequency (328 Hz) due to the membrane stiffness.

To study the impact of membrane thickness and material on resonance frequency, eigenfrequency analyses were conducted for varying thicknesses and Young's moduli, keeping the bubble radius constant. As observed in Figure 12, increasing the thickness of stiff membranes raises the resonance frequency. In contrast, for soft membranes, thicker membranes lower the resonance frequency, resembling free bubble behavior where resonance decreases with increasing radius ($E/E_s = 0$).

As a final investigation, the resonance frequency of different bubble shapes with the same volume is evaluated. To that end, three geometries are considered: ellipse, cylinder, and snowman. Figure 13 shows the dimensions of each geometry and their corresponding pulsation modes. Interestingly, the ellipsoid bubble demonstrates a lower resonance frequency in comparison to the spherical bubble even when both geometries have the same volume. This is explained by the excitation in the direction of the shorter side of the ellipsoid bubble.

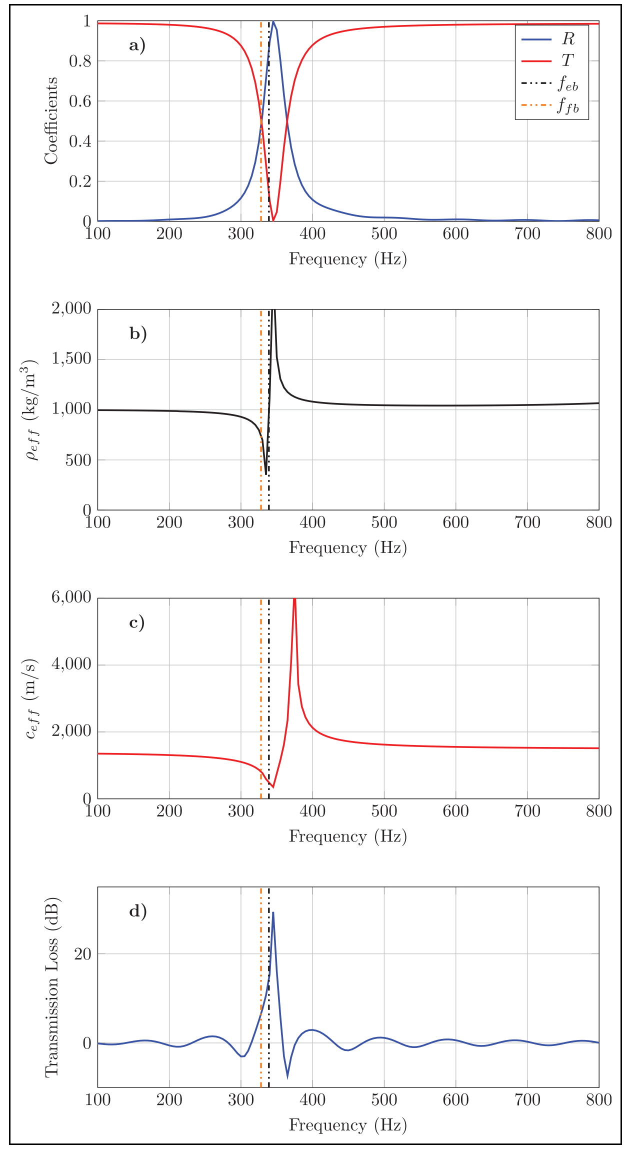

Figure 11. (a) Reflection and transmission coefficients obtained through equations (17) and (18), (b) Effective mass density, (c) effective phase velocity, and (d) transmission loss for an air bubble of radius $r_b = 1$ cm encapsulated by a silicone membrane of thickness $r_s = 2$ mm. The black and orange vertical lines indicate the resonance frequency predicted by the eigenfrequency analysis for the encapsulated (f_{eb}) and free bubble (f_{fb}), respectively.

The effective acoustic properties of these bubble designs are also retrieved, which are exhibited in Figures 14 to 16. The main peaks observed in the effective acoustic properties are attributed to the resonance modes identified through eigenfrequency analysis, although the peaks are shifted due to boundary conditions of the finite medium in contrast to a infinite

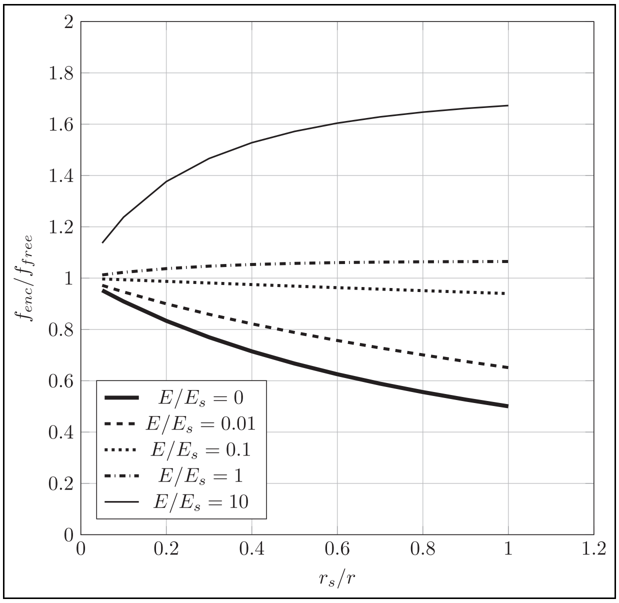

Figure 12. Effect of membrane thickness and material on the resonance frequency of the encapsulated bubble. The thick solid back curve ($E/E_s = 0$) shows the resonance frequency for a free air bubble case with an increment in the bubble radius.

medium from the eigenfrequency study. For the ellipsoid bubble (Figure 14), two distinct peaks are observed corresponding to the two pulsation modes; one identified in Figure 13(a), while the second refers to a mode that excites the shorter dimension of the bubble of frequency 313 Hz. Finally, for the cylindrical bubble (Figure 16), one main peak is observed near the pulsation mode of 463 Hz. The cylindrical and snowman geometries similarly exhibit multiple resonance peaks due to their non-spherical modes. In all cases, the black vertical lines in the figures indicate the eigenfrequency predictions, confirming the correspondence between the modal analysis and the retrieved effective properties.

Vibroacoustic model for underwater noise prediction

To verify the performance of the meta-curtain on reducing underwater noise, a numerical vibroacoustic axisymmetric model based on the benchmark test COMPILE I (Lippert et al., 2016) is analyzed through Comsol Multiphysics. This benchmark test has been

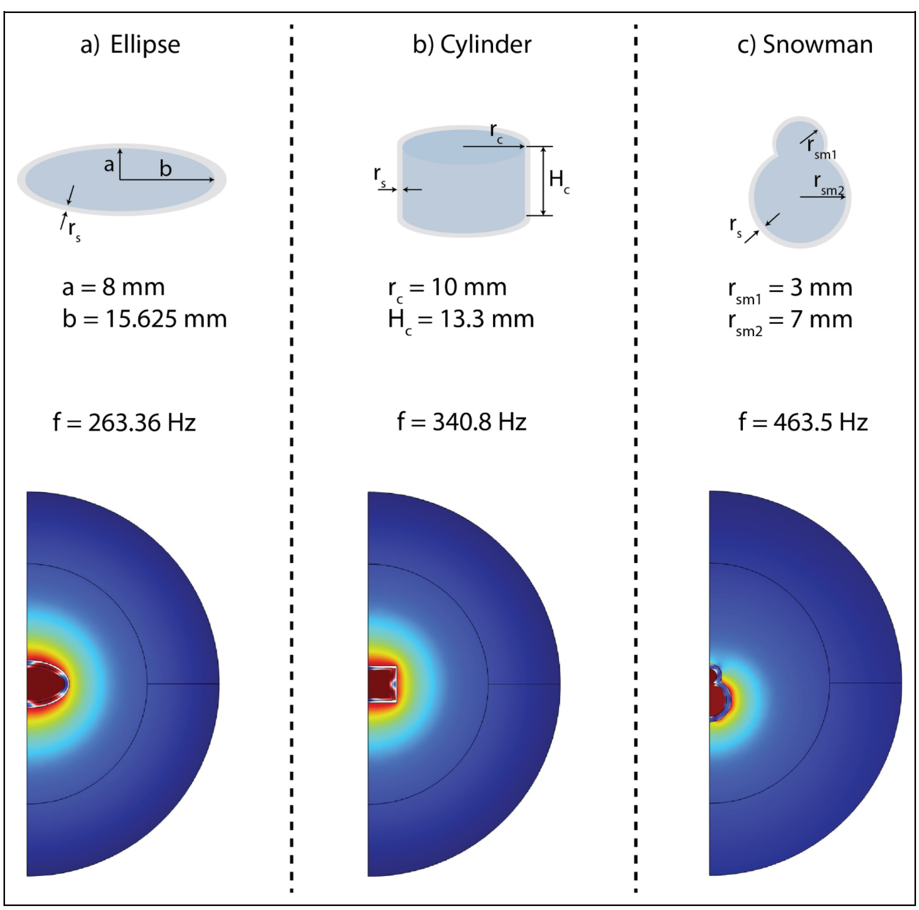

Figure 13. Dimensions and resonance frequencies of bubbles of geometries: (a) ellipse, (b) cylinder, and (c) snowman. All geometries have the same volume and thickness r_s of the spherical encapsulated bubble from Figure 10.

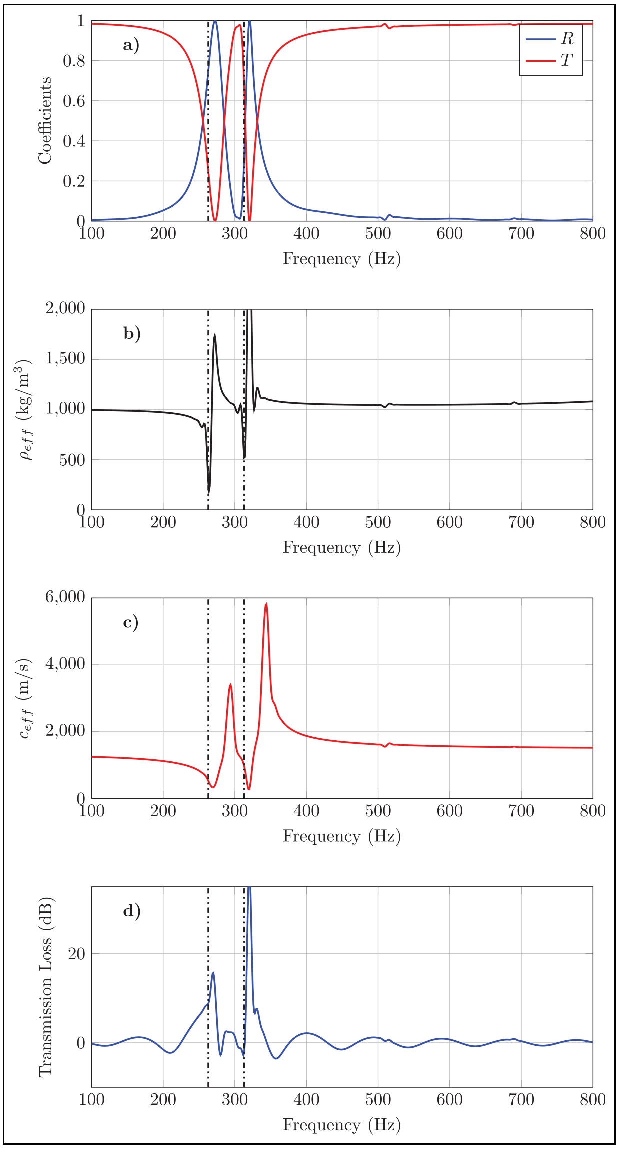

Figure 14. (a) Reflection and transmission coefficients obtained through equations (17) and (18), (b) Effective mass density, (c) effective phase velocity, and (d) transmission loss for an ellipsoid air bubble with dimensions presented in Figure 13 encapsulated by a silicone membrane of thickness r_s = 2 mm. The black lines indicate the resonance frequency predicted by the eigenfrequency analysis.

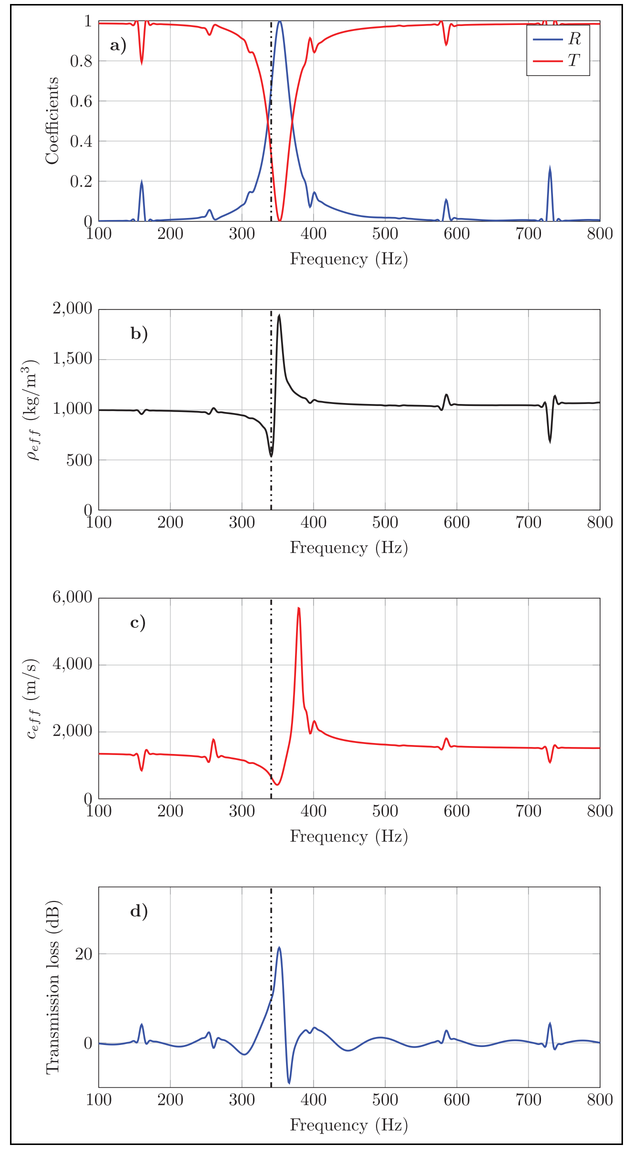

Figure 15. (a) Reflection and transmission coefficients obtained through equations (17) and (18), (b) Effective mass density, (c) effective phase velocity, and (d) transmission loss for an cylindrical air bubble with dimensions presented in Figure 13 encapsulated by a silicone membrane of thickness r_s = 2 mm. The black lines indicate the resonance frequency predicted by the eigenfrequency analysis.

widely applied to evaluate the ability of numerical models to replicate the effects of underwater sound generated by an impact-driven pile. The model consists of a pile with a length of $L = 25$ m, having an embedded length of $L_s = 15$ m, as shown in Figure 17(a). The pile has an outer diameter of $D = 2$ m and wall thickness $t = 0.05$ m. The water and soil are modeled as acoustic media, allowing only the propagation of pressure waves, while perfectly matched layers (PML) are introduced to reduce the wave reflection in both media. Modeling the seabed as an acoustic medium is only acceptable when the soil has a much lower shear wave speed than compressional waves (Tsouvalas, 2020). Damping effects are only applied at the soil and the embedded pile section. The impact force generated by the hammer strike is modeled as an exponential function defined according to the hammer features. More information about the properties can be found in Lippert et al. (2016).

Modeling the actual geometry of the meta-curtain in the vibroacoustic model would increase expressively the computational time. Since the incident acoustic

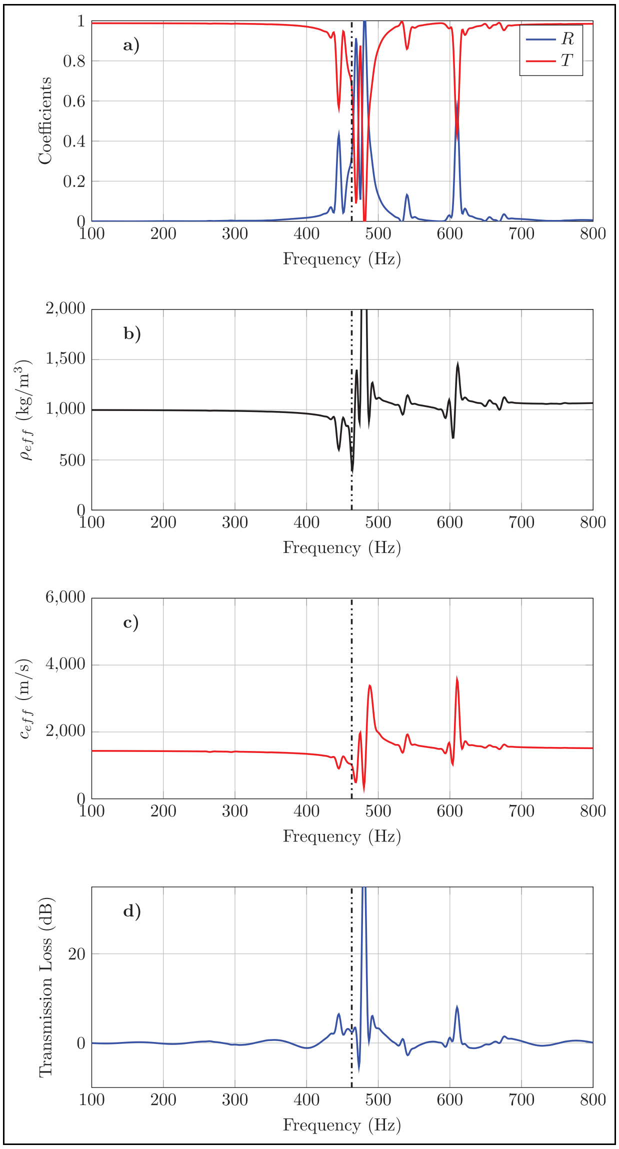

Figure 16. (a) Reflection and transmission coefficients obtained through equations (17) and (18), (b) Effective mass density, (c) effective phase velocity, and (d) transmission loss for an snowman air bubble with dimensions presented in Figure 13 encapsulated by a silicone membrane of thickness $r_s = 2$ mm. The black lines indicate the resonance frequency predicted by the eigenfrequency analysis.

wavelength is longer that the bubble size and the amplitude of the acoustic wave is small, the meta-curtain can be replaced by a uniform layer containing effective acoustic properties determined in the previous section – the effective mass density and effective phase velocity (Gao et al., 2021).

As output of the numerical simulations, the acoustic pressure time series $p_0(t)$ are measured at the sampling points, which are further used to calculate the sound exposure level SEL and zero-to-peak sound pressure level $\mathrm{SPL}_{p,pk}$, defined as

$$\mathrm{SEL} = 10\log\left(\frac{E_{90}}{0.9p_0^2 1s}\right)[\mathrm{dB}], \tag{22}$$

$$\mathrm{SPL}_{p,pk} = 10\log\left(\frac{\max(p^2)}{p_0^2}\right)[\mathrm{dB}]. \tag{23}$$

Figure 18(a) presents the acoustic pressure time signal measured at a position of $r = 11$ m and $z = 5$ m by using the Comsol numerical model. The signal agrees well with the one presented in Lippert et al. (2016). A bubble curtain with effective mass density $\rho_{\mathrm{eff}} = 990$ kg/m^3 and effective phase speed $c_{\mathrm{eff}} = 218$ m/s was placed around the monopile at the distance of $r = 10$ m from the noise source. Figure 18(b) depicts the acoustic pressure time signal measured at the same position, from which a significant reduction in pressure level is observed; the maximum peak level drops by slightly more than half in comparison to the case without curtain. The extra peaks observed in the meta-curtain case arise from the interaction of the sound waves with the curtain domain, which generate several wave reflections.

The vibroacoustic model employs linear acoustic assumptions, which are justified for the following reasons. At the meta-curtain deployment distance of $r = 10$ m from the pile, the acoustic pressure amplitudes have decayed sufficiently for linear theory to apply. The COMPILE I benchmark (Lippert et al., 2016), which uses the same assumptions, has been validated against field measurements of pile-driving noise at comparable distances. The transient pile-driving signal is decomposed into frequency components, and the attenuation at each frequency is evaluated using the frequency-dependent effective properties from Section “Effective acoustic properties of the meta-curtain,” under the superposition principle valid in the linear regime (Figure 18). For meta-curtain configurations placed within 1–2 m of the pile, nonlinear acoustic effects may become relevant, and the linear assumption would require reassessment.

Experimental analysis of bubbles in small scale tank setup

Experimental setup

To verify the functionality of the encapsulated bubbles, three bubble designs are prototyped and tested in a small scale tank setup; the spherical (Figure 10), ellipsoid (Figure 13(a)), and cylindrical (Figure 13(b)) bubbles. In this section, the experimental setup is described, where the required instrumentation for generating and measuring the underwater sound is introduced, as well as its positioning inside the tank based on the wavelengths of interest. Since the focus of this project is on attenuating sounds of frequencies lower than 1 kHz, the resonance frequency of the proposed encapsulated

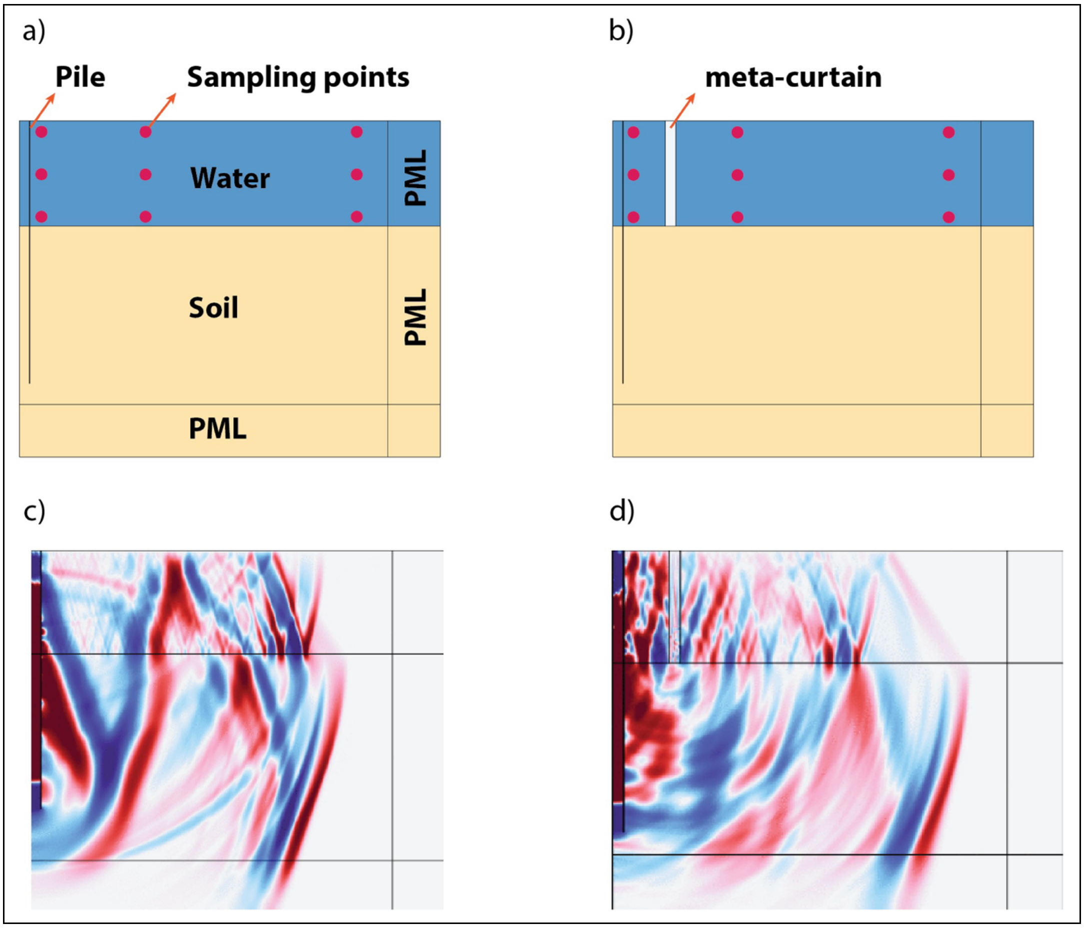

Figure 17. Numerical vibroacoustic axisymmetric model to predict the sound levels of impact-driven piles (a) without a meta-curtain and (b) with a meta-curtain. Screenshot of pressure field of the model (c) without the meta-curtain and (d) with the meta-curtain.

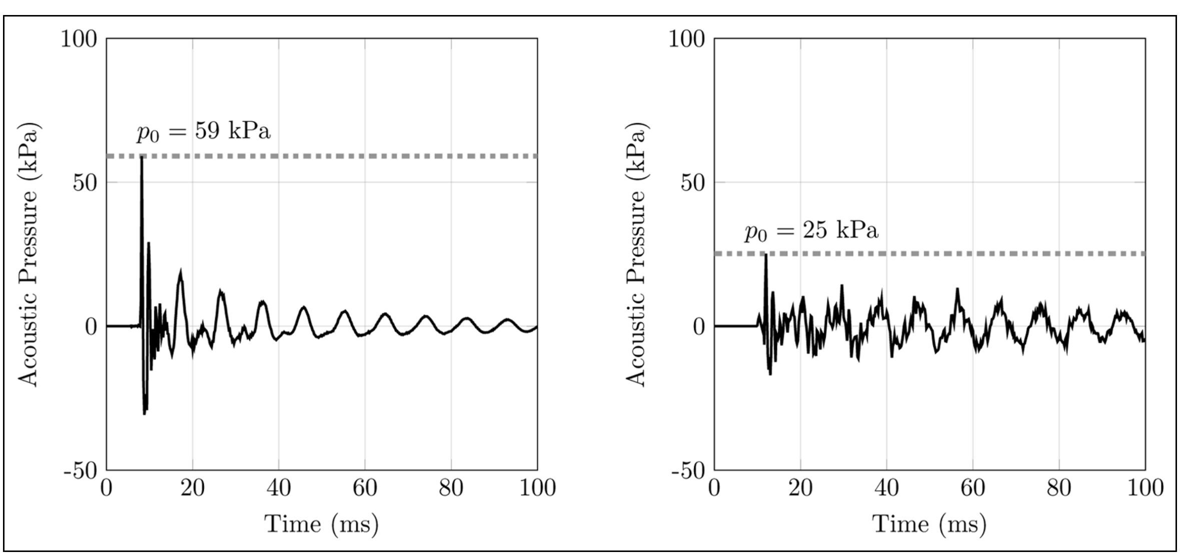

Figure 18. Acoustic pressure measure at position for a pile system (a) without curtain and (b) with curtain. The horizontal line indicates the maximum pressure level identified in each curve.

bubbles is located inside this range. Then, the manufacturing process of the encapsulated bubbles is introduced. Finally, the bubbles are assembled and placed inside the tank for testing.

The schematic of the tank setup indicating the sensors' position is shown in Figure 19(a). Since the tank length has dimension 140 m, here only the working area (middle part) is highlighted. The remaining tank dimensions are 4.3 m in width and 2.3 m in depth. An underwater speaker Aqua-30 (rated power of 30 W) is positioned at the center of the tank. Three hydrophones are used to measure the sound before and after the curtain, being two of them (H1 and H3) aligned with the speaker position and the remaining (H2) aligned with hydrophone H1. The distance between hydrophones H1 and H2 and the curtain will be shifted between 1 and 2 m. Amplifiers VP2000 are used to increase the signal gain to 30 dB and to filter signals outside the range of interest – a lowpass filter of 5 kHz is applied. The hydrophones are calibrated before positioning inside the tank with the aid of a calibrator, as indicated in III) in Figure 19(b). The hydrophone specifications and sensitivities are presented in Table 1.

Two types of sound signal are used to evaluate the functionality of the meta-curtain. The first consists of a sweep signal of duration 10 s, covering a frequency range between 100 and 2000 Hz, where the resonance frequencies of the bubbles are located. The second signal is a pink noise of same duration; this signal is characterized by a power spectral density that is inversely proportional to the signal frequency, resulting in equal energy per octave of frequency. Both signals are generated through a Matlab script and sent to the underwater speaker. The sound recorded by the hydrophones are sent to the DAQ (Figure 19(b)) for analysis.

Prototyping of bubbly membranes

Manufacturing individual encapsulated bubbles demands time and increases complexity of assembling them inside the tank. To overcome such limitations, we propose the fabrication of rectangular silicone membranes with several embedded air bubbles, which will be known as bubbly membranes. The steps for manufacturing the bubbly membranes are introduced in Figure 20. The moldings used to fabricate the bubbly membranes are 3D printed in two parts; the top and bottom plates that forms the cavity with the designed geometry. The Ecoflex 00-35 rubber silicone was used due to its fast curing time (5 min). The silicone is made by mixing two agents (parts A and B) with the same aspect ratio (1:1). The silicone is poured into the bottom plate. The top plate is placed and pressed against the bottom plate and kept until the silicone is fully cured. This process creates one-half of the bubbly membrane containing half of the design cavities. The process is repeated to create the second half, then the two parts are glued together using a thin layer of silicone. After curing, the resulting membrane will contain closed cavities in atmospheric pressure. The manufacturing process is repeated for the spherical and ellipsoid bubble designs, which resulted in 15 membranes containing four spherical bubbles, 15 membranes containing four ellipsoid bubbles, and 7 membranes containing 16 cylindrical bubbles. Notice that the molding designs for these two geometries are distinct from the cylindrical-shaped bubbles, due to the availability of 3D printing machines.

Bubbly membranes assembling

The manufactured bubbly membranes were arranged in two distinct configurations, as shown in Figure 21, to evaluate the meta-curtain performance. Configuration 1 uses only the spherical and ellipsoid membranes to assess their attenuation near the respective resonance frequencies (340 Hz for spherical, 263 Hz for ellipsoid). Configuration 2 combines all membrane types (spherical, ellipsoid, and cylindrical) to evaluate whether broader-band attenuation can be achieved by exploiting the different resonance frequencies of each bubble geometry. In both configurations, the membranes were attached to the ropes using screws, nuts, and washers. A bottom aluminum beam was used to keep the membranes straight when submerged, while for configuration 2 two vertical beams were also added to avoid floating.

Analysis of sweep signal noise

Background noise. Before measuring the sound levels with the tank containing the meta-curtain, the background noise is first recorded, as shown in Figure 22. This provides a reference for hydrophone measurements without the curtain and helps assess the efficiency of the curtain. All the results in this section are presented as one-third octave bands.

Analysis of meta-curtain with single membranes. Figure 23 shows the octave band for meta-curtains formed by single spherical membranes (Figure 23(a)) and by single ellipsoid membranes (Figure 23(b)) when interacting of a sweep signal noise. As a first observation, the sound levels for systems containing single membranes at frequencies around 800 Hz drop in comparison to the background noise case, where levels near 220 dB are measured at hydrophone H3. This may occur due to reduction in wave reflections caused by the meta-curtain placement.

Near the resonance frequencies of both bubbles, however, the sound levels before and after the curtain are similar – possibly due to the narrow resonance range not being captured in the one-third octave band

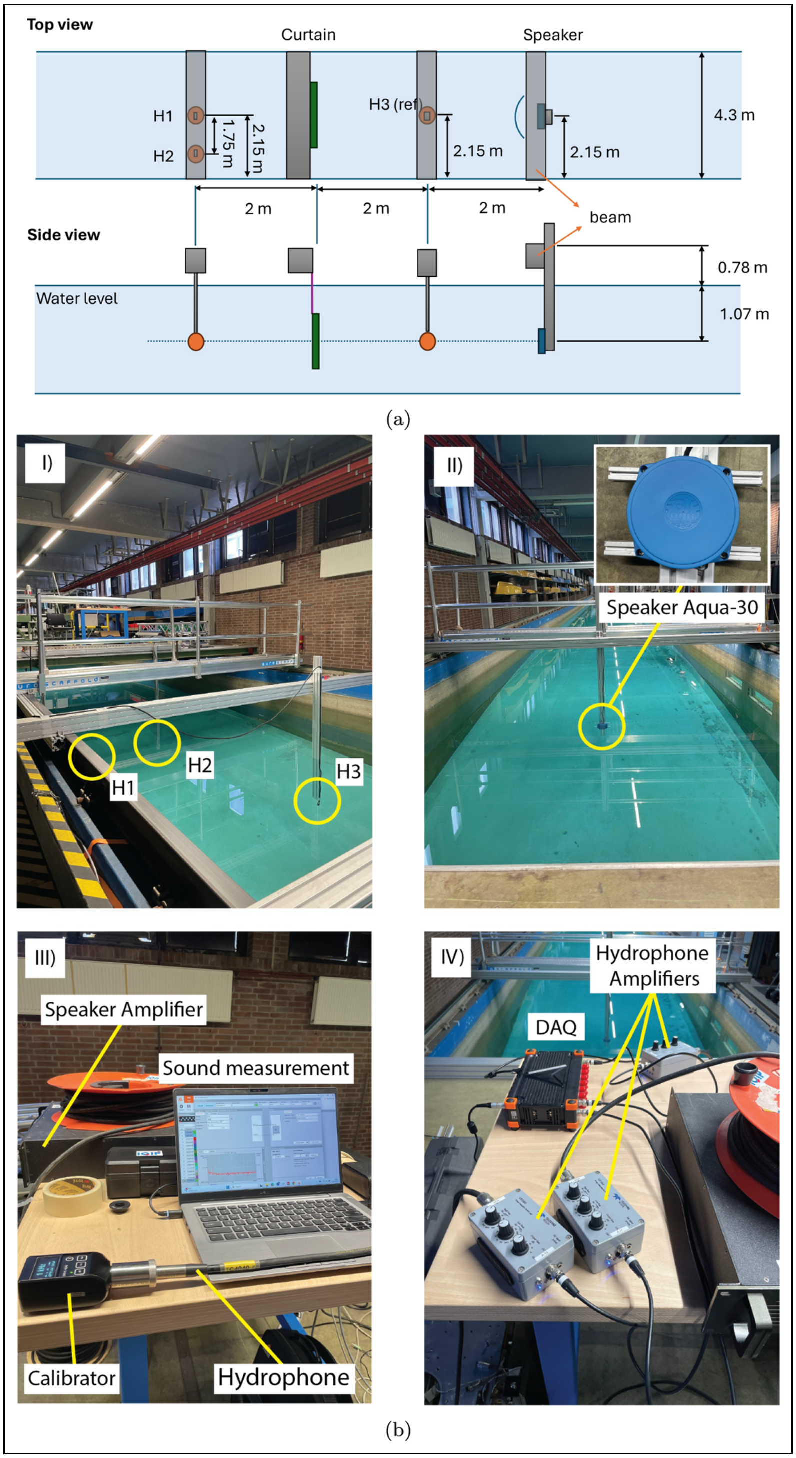

Figure 19. (a) Sketch of the experimental setup for evaluating the meta-curtain performance. (b) Installation of sensors in the tank: (I) hydrophones positioning and references; (II) underwater speaker; (III) and (IV) hydrophone calibration and amplifiers for hydrophones and speaker.

analysis. Other possible reasons could be the small amount of bubbles placed in the tank cross section – the several empty areas between the bubbly membranes allow the wave propagation – and the single curtain layer in the direction of the sound wave propagation.

Analysis of meta-curtain with combined membranes. Since one of the possible causes of the small wave attenuation at the bubble resonance frequency could be the use of few bubbly membranes, the next analysis shows the results for a meta-curtain containing all fabricated

Table 1. Technical information of the hydrophones.

Hydrophone	Model	Frequency range	Sensitivity
H1	TC4040-7	1 Hz–120 kHz	0.9844764 mV/Pa
H2	TC4040-4	1 Hz–120 kHz	1.357919 mV/Pa
H3	TC4040-4	1 Hz–120 kHz	1.38236 mV/Pa

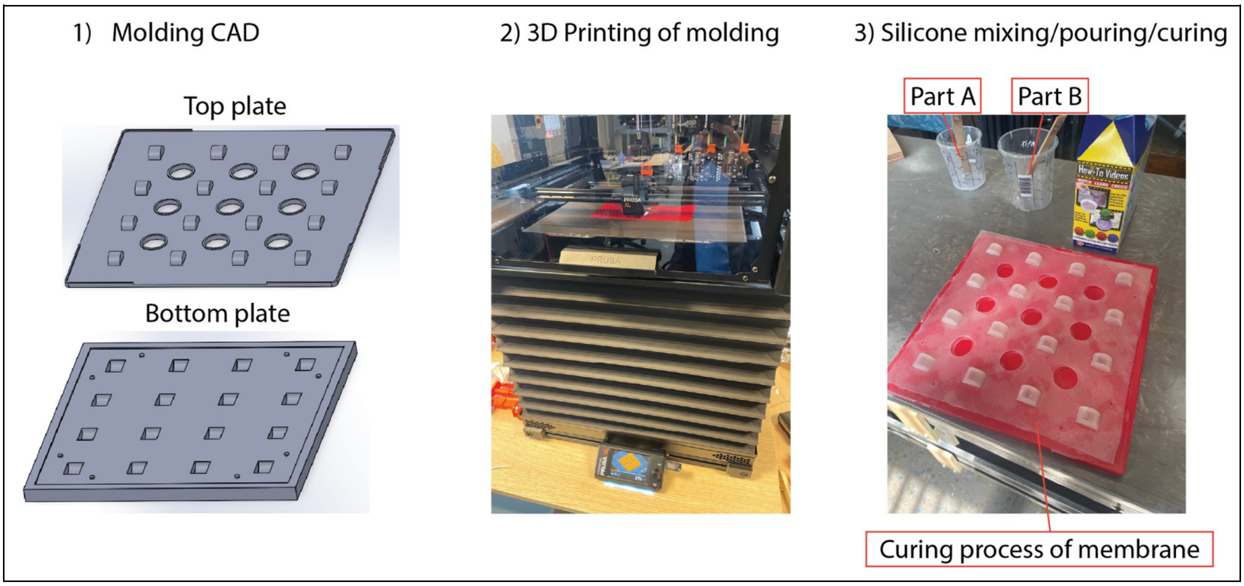

Figure 20. Manufacturing steps for the bubbly silicone membranes.

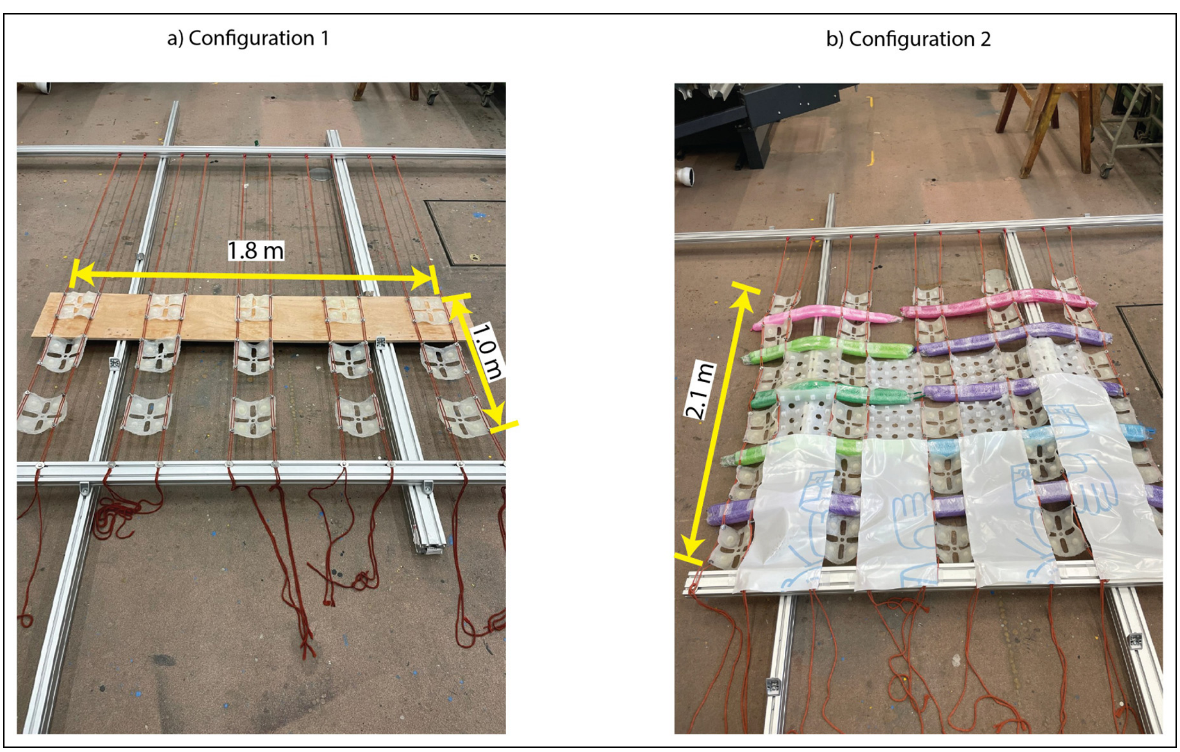

Figure 21. Meta-curtain configurations for validating principle. (a) Configuration 1 is used to test the principle of the small membranes containing spherical and ellipsoid bubbles; (b) Configuration 2 is used to test the principle of all membranes combined.

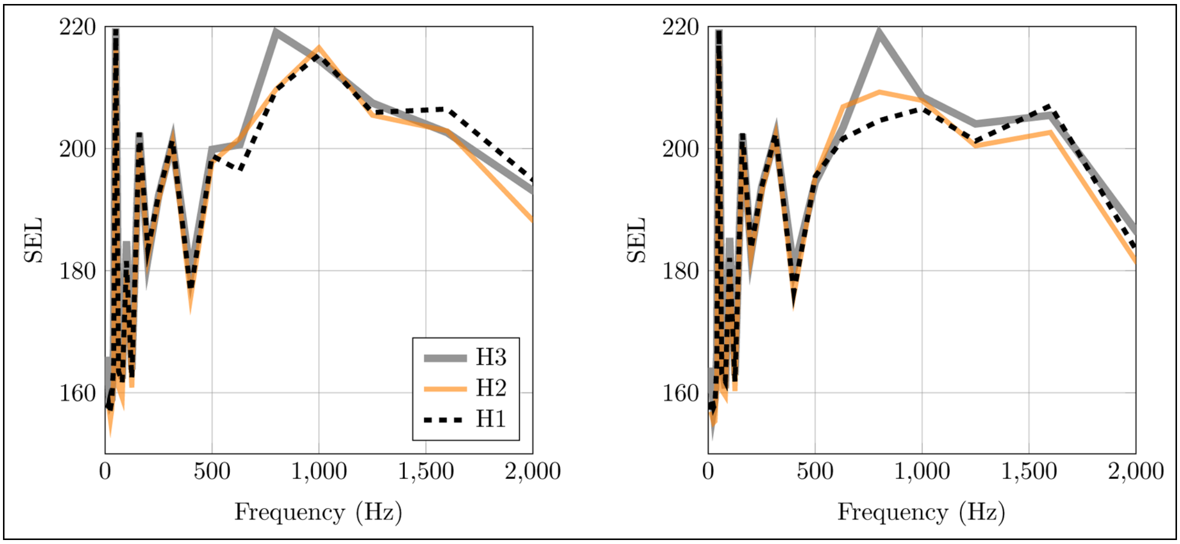

Figure 22. Sound measured at the hydrophones for a system without curtain. Hydrophones H1 and H2 are placed at (a) 1 m and (b) 2 m from the curtain position.

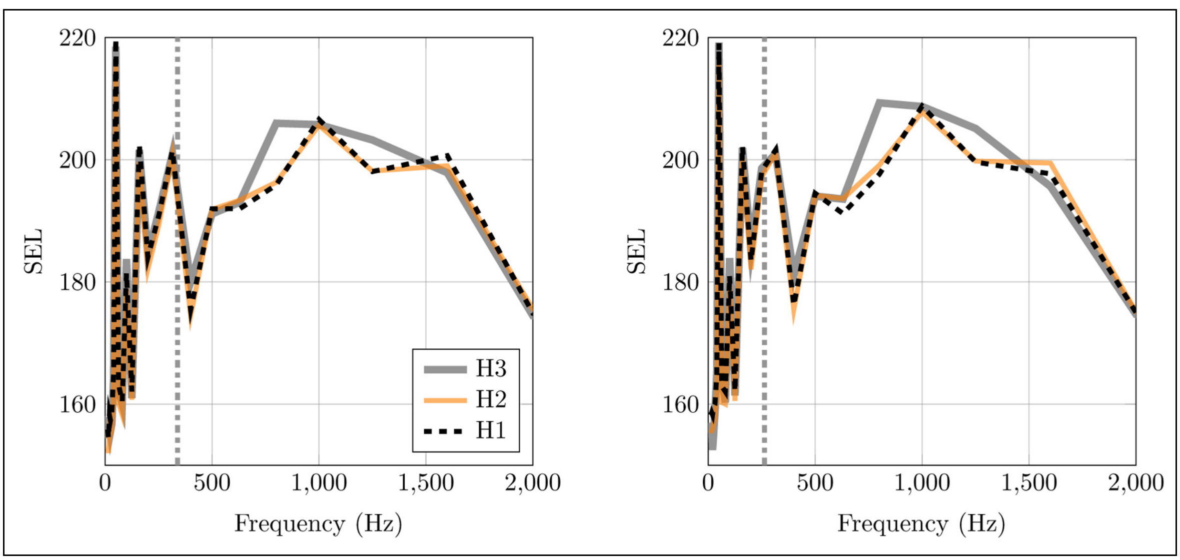

Figure 23. Sound measured at the hydrophones for a curtain with single membranes containing (a) spherical bubbles and (b) ellipsoid bubbles. Sound levels are measured at 2 m from the curtain.

membranes, which duplicated its height, as shown in Figure 21–notice that due to the presence of empty spaces between the bubbly membranes, long balloons filled with air were attached to the frame. Figure 24 shows the octave band for meta-curtains formed by all membranes and long balloons.

Interestingly, a SEL peak around 400 Hz appears, which was not observed in previous simulations. This could be explained by reflections caused by the long balloons. Measurements at hydrophones H1 and H2 show a reduction level of around 15 dB near the bubble resonance frequencies. For measurements near the curtain (Figure 24(a)), hydrophone H1 records lower SEL values than hydrophone H2 at frequencies above the resonance. In contrast, for measurements farther from the curtain (Figure 24(b)), both hydrophones show similar SEL levels, suggesting wave reflections inside the tank.

Tests were also performed for the case of the curtain with all the bubbly membranes without the long balloons, from which results are depicted in Figure 25. Notice that the SEL peak around 400 Hz disappears, which could confirm that it appears due to the long balloons effect. The sound levels are slightly reduced around the bubbles' resonance frequencies.

To compare the attenuation performance of the meta-curtain with other noise mitigation strategies, a

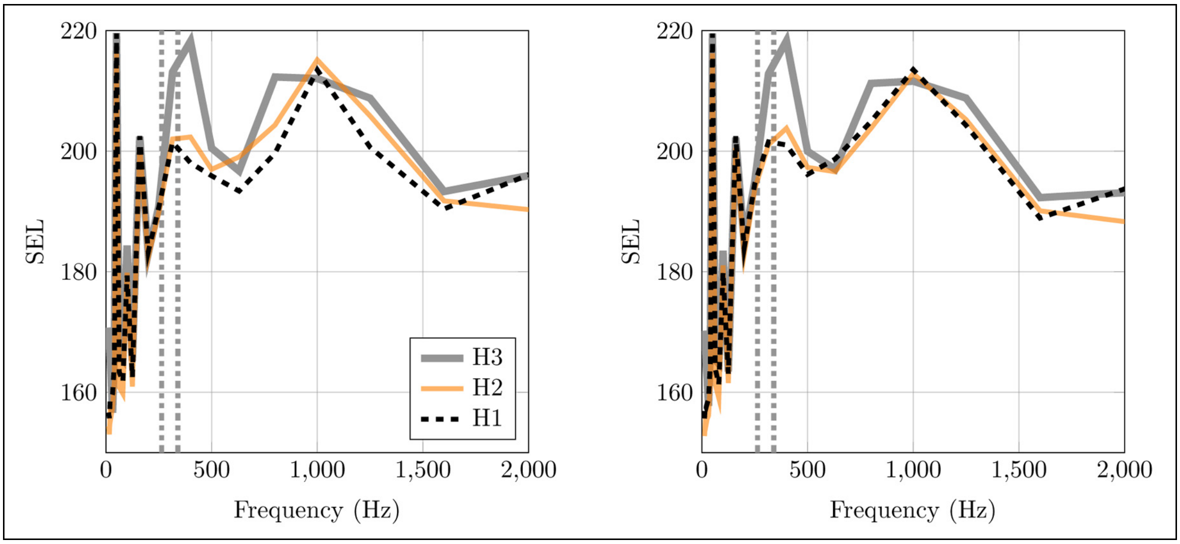

Figure 24. Sound measured at the hydrophones for a curtain containing all membranes and long balloons. Hydrophones H1 and H2 are placed at (a) 1 m and (b) 2 m from the curtain position.

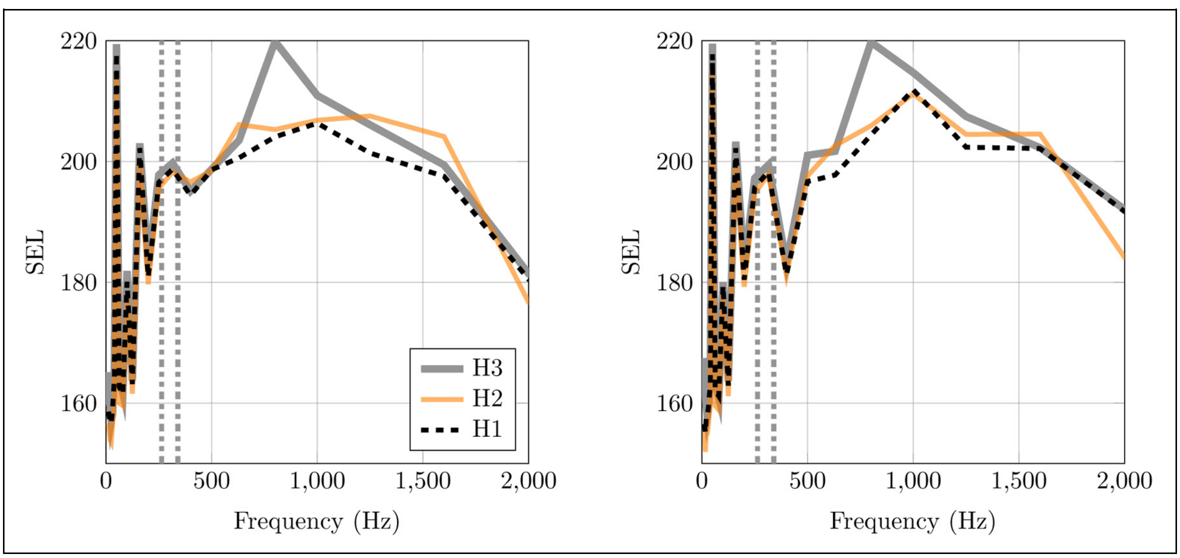

Figure 25. Sound measured at the hydrophones for a curtain containing only bubbly membranes. Hydrophones H1 and H2 are placed at (a) 1 m and (b) 2 m from the curtain position.

foam layer has been placed in front of the meta-curtain. Figure 26 shows the octave band for meta-curtains formed by all membranes, long balloons, and the foam layer. The addition of a foam only introduced some sound attenuation around 1200 Hz, while for lower frequencies, the sound levels kept at almost the same levels.

Analysis of pink noise

Background noise. Taking into account a speaker that emits pink noise inside the tank, the background noise is first measured, which is presented in Figure 27. For frequencies higher than 500 Hz, it is observed slightly constant sound levels around 185 dB. Once again, these measurements are used as reference for the evaluation of sound levels for a tank containing the curtain prototypes.

Analysis of meta-curtain with single membranes. Figure 28 shows the octave band for meta-curtains formed by single spherical membranes (Figure 28(a)) and by single ellipsoid membranes (Figure 28(b)) when interacting of a pink noise signal. The sound levels measured by hydrophone H3 on the background (BG) case are also included for better comparison. Similarly to the case with the sweep signal, it is not noticed sound

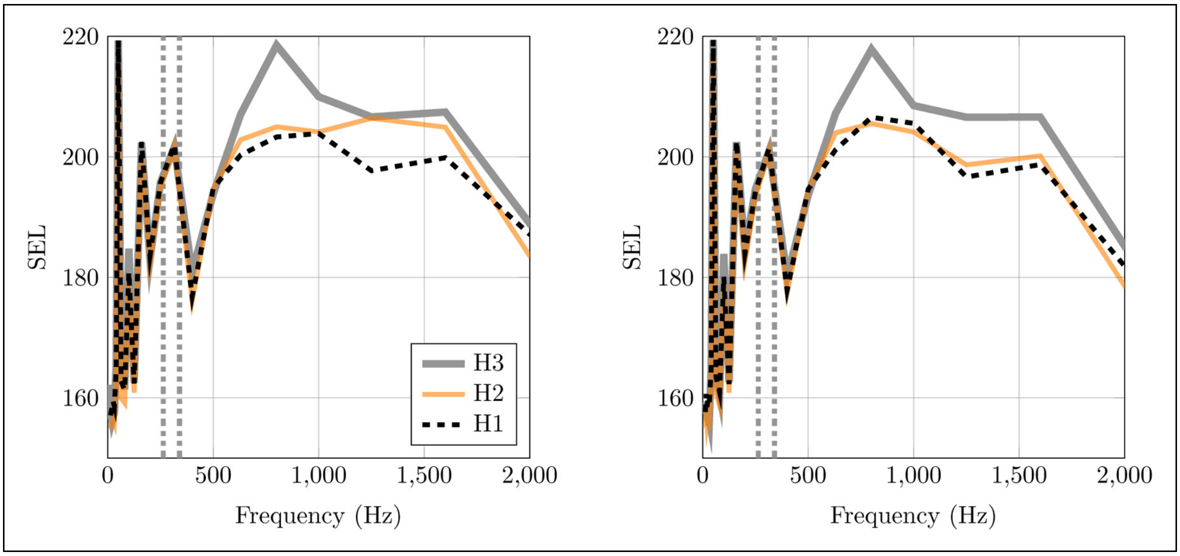

Figure 26. Sound measured at the hydrophones for a curtain containing all membranes, long balloons, and foam. Hydrophones H1 and H2 are placed at (a) 1 m and (b) 2 m from the curtain position.

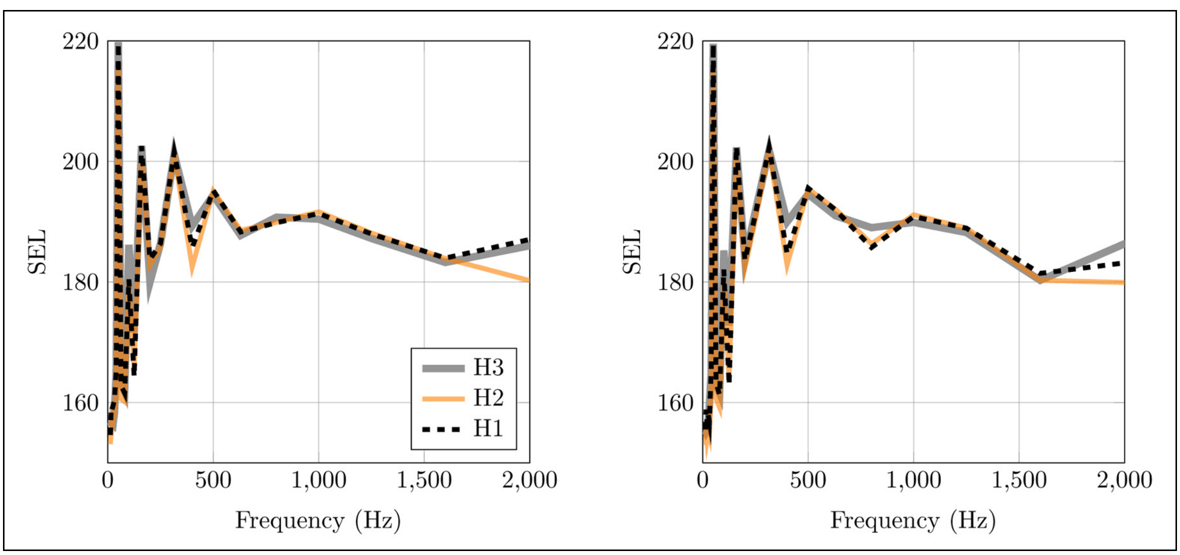

Figure 27. Sound measured at the hydrophones for a system without curtain due to pink noise emission. Hydrophones H1 and H2 are placed at (a) 1 m and (b) 2 m from the curtain position.

attenuation at the bubbles resonance frequency, which could be explained by the same reasons from the previous case.

Analysis of meta-curtain with combined membranes. Figure 29 shows the octave band for meta-curtains formed by all membranes and long balloons, where a significant drop is observed around 800 Hz, being possible be influenced by the long balloons presence.

Measurements are again performed without the long balloons, as shown in Figure 30. Unlike the previous case, no reduction is observed around 800 Hz, suggesting the influence of the long balloons in that frequency range. Additionally, the sound levels near the bubbles' resonance frequencies are slightly lower compared to both reference hydrophone H3 and the background noise case.

Figure 31 shows the octave band for meta-curtains formed by all membranes, long balloons, and foam. Similarly to the case for the sweep noise, a significant attenuation is observed at a frequency range near 400 Hz.

Insertion loss analysis

In the insertion loss analysis, the sound levels measured by a hydrophone for both no curtain and curtain cases

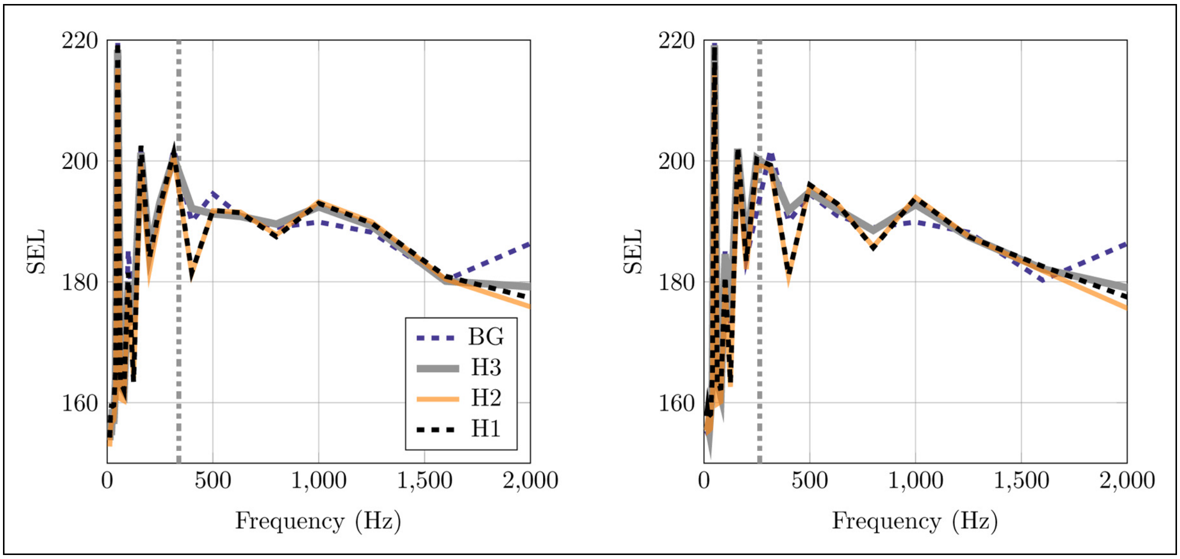

Figure 28. Sound measured at the hydrophones for a curtain with single membranes containing (a) spherical bubbles and (b) ellipsoid bubbles due to pink noise emission. Sound levels are measured at 2 m from the curtain. The sound measured at hydrophone H3 for the background case are also included for reference.

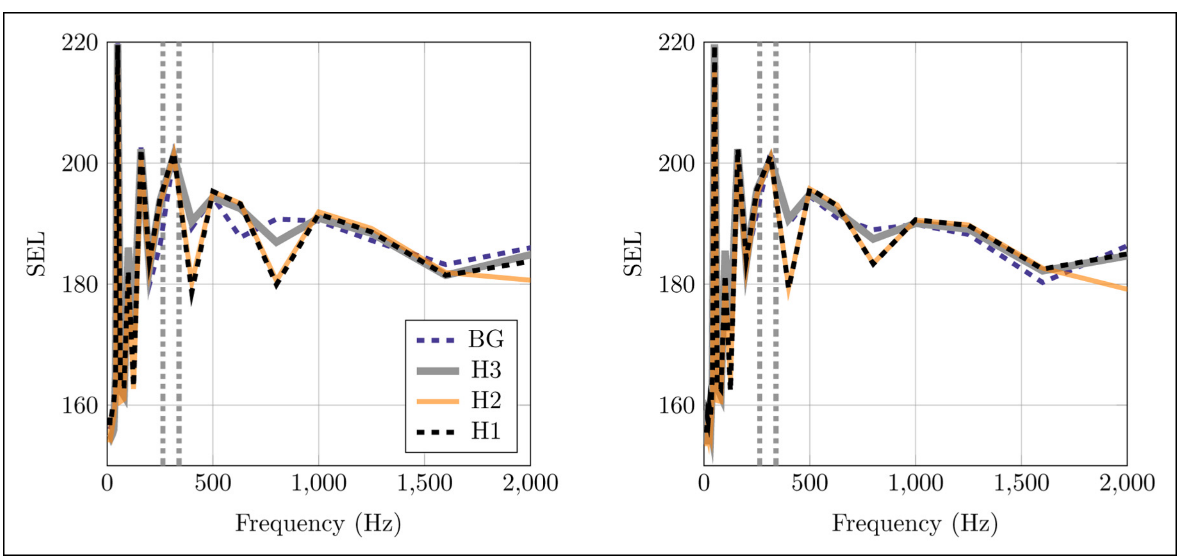

Figure 29. Sound measured at the hydrophones for a curtain containing all membranes and long balloons due to pink noise emission. Hydrophones H1 and H2 are placed at (a) 1 m and (b) 2 m from the curtain position.

are compared to each other. In this section, the measurements of hydrophones H1 and H3 are presented for both noise sources, from which the transmission and reflection abilities are evaluated.

Analysis of meta-curtain with single membranes. Figures 32 and 33 show the insertion loss for the cases of single curtains containing spherical and ellipsoid bubbles, respectively. The sound levels are measured at a distance of 2 m from the curtain. Here, the sound levels for the curtain cases at the bubbles' resonance frequency are slightly lower than the case without curtain. However, after the resonance frequency, higher attenuation levels are observed, especially for measurements related to the sweep signal.

Analysis of meta-curtain with combined membranes. Figure 34 shows the insertion loss for the measurements at 1 m for the curtain case with all membranes and long balloons. For the sweep signal measurements, the sound attenuation is observed for frequencies higher than 500 Hz.

Figure 35 shows the insertion loss for the measurements at 1 m for the curtain case with only membranes, where the resonance effect is relatively noticeable in

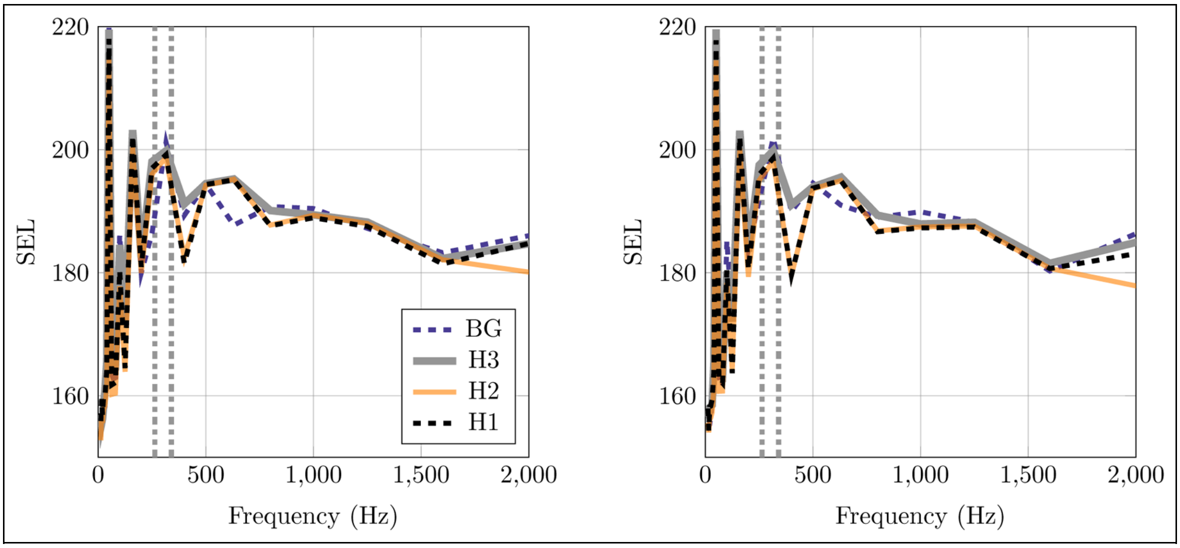

Figure 30. Sound measured at the hydrophones for a curtain containing only bubbly membranes due to pink noise emission. Hydrophones H1 and H2 are placed at (a) 1 m and (b) 2 m from the curtain position.

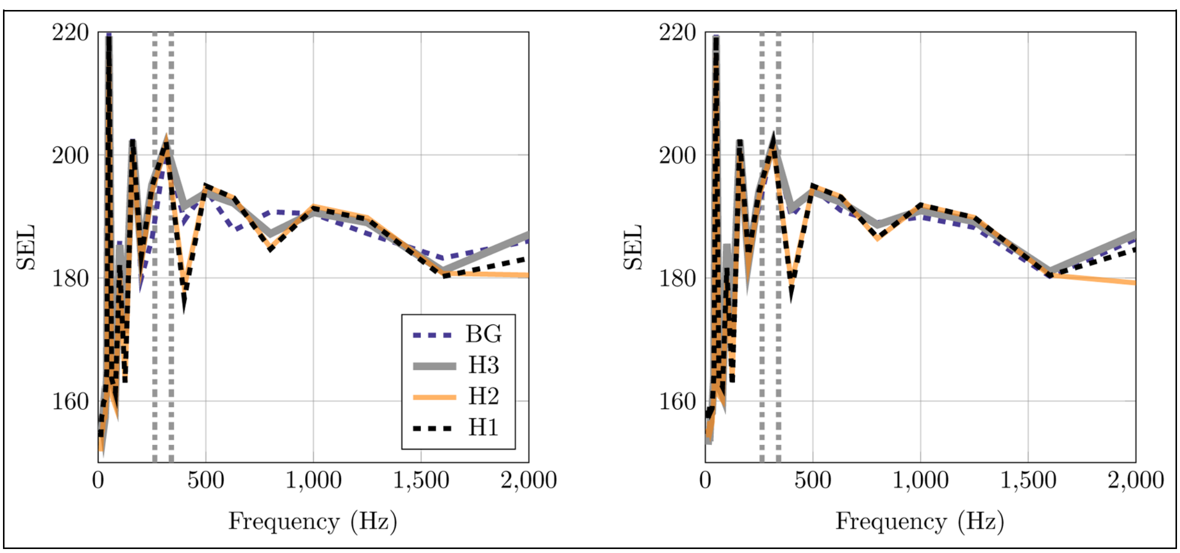

Figure 31. Sound measured at the hydrophones for a curtain containing all membranes, long balloons, and foam due to pink noise emission. Hydrophones H1 and H2 are placed at (a) 1 m and (b) 2 m from the curtain position.

comparison to the results in Figure 34. For frequencies higher than 500 Hz, the sound levels reduce significantly, especially for the sweep signal case.

Figure 36 shows the insertion loss for the measurements at 1 m for the curtain case with all membranes, long balloons, and foam. As a first observation, the resonance effect is not noticeable, which could be explained by the influence of the foam layer. The sound level reduces expressively for higher frequencies.

Conclusions and recommendations

This paper presented a three-step design methodology to explore the attenuation mechanisms of the metacurtain through theoretical, numerical, and experimental analyses. The bubble attenuation is evaluated using established theoretical and numerical models, supported by water tank experiments on bubble prototypes. This section summarizes the key findings and offers recommendations for the next design steps.

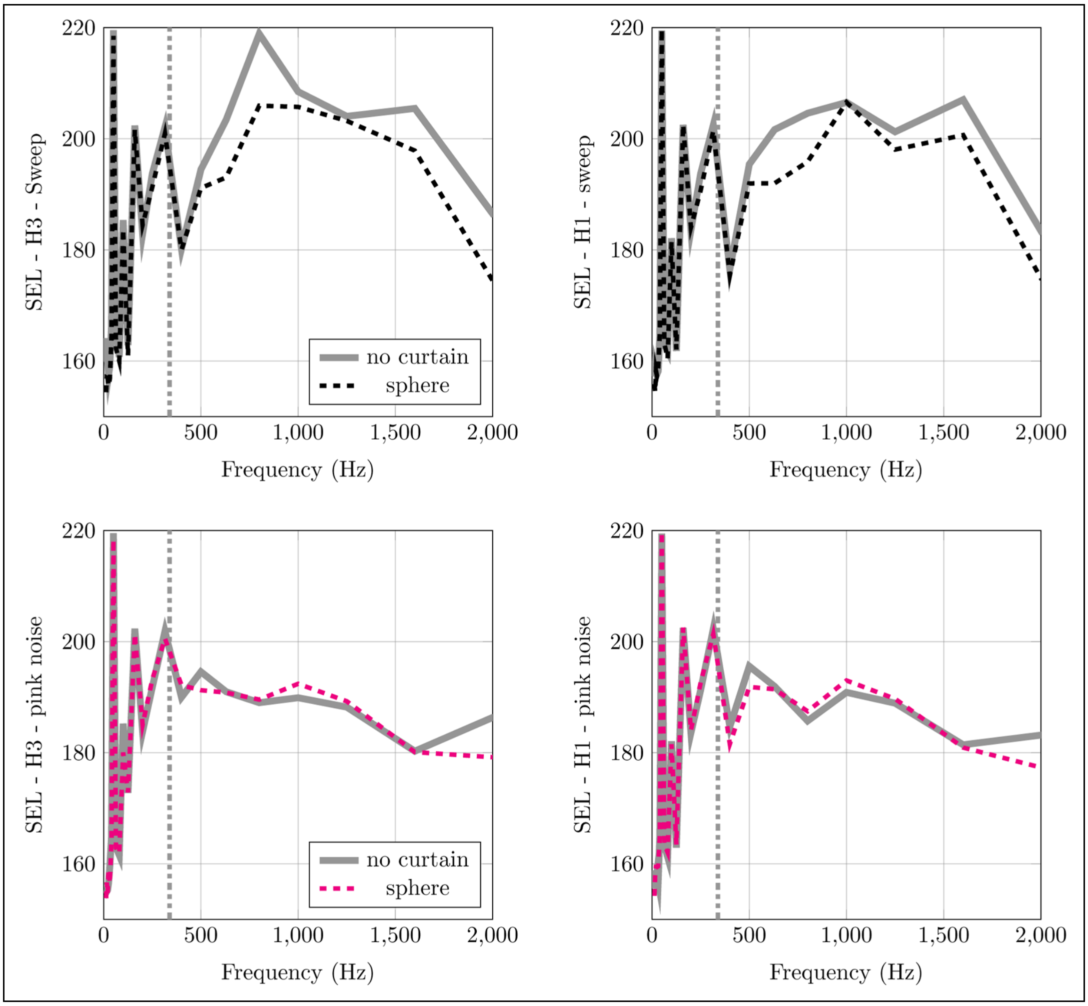

Figure 32. Insertion loss of a membrane containing spherical bubbles. Measurements presented in (a and b) are related to the sweep signal at hydrophones H3 and H1, while measurements at (c and d) are related to the pink noise signal at hydrophones H3 and H1.

Numerical simulations showed that bubble resonance significantly affects acoustic properties, as seen in the frequency-dependent behavior of effective mass density and phase speed. Designs such as ellipsoid and snowman bubbles exhibit multiple resonance modes, which may offer broader attenuation bandwidth compared to traditional spherical bubbles. The ellipsoid bubble, in particular, demonstrates a lower primary resonance frequency (263 Hz while 340 Hz for the sphere) at the same volume fraction. The choice of encapsulating membrane also plays a critical role – thicker, flexible membranes can mimic the resonance of free bubbles. Exploring such designs with flexible encapsulation can enhance acoustic performance across a wider frequency range, as demonstrated by the multiple resonance peaks observed in Figures 14 to 16, particularly at low frequencies relevant to offshore pile installation.

The molding and pouring process proved practical for manufacturing bubbly membranes, enabling the simultaneous production of multiple bubbles – especially with large 3D-printed molds. These molds must be robust enough to withstand demolding without damage. The process also supports the use of various silicone materials with different flexibilities, allowing tuning of resonance frequencies. This flexibility is essential when designing bubbles for varying water depths, where underwater pressure significantly affects bubble shape.

Experimentally, the bubbly membranes attenuated noise at frequencies above their resonance, as predicted by theoretical models. However, attenuation near the resonance frequency was limited, likely due to an insufficient number of bubbly membranes in the tank cross-section or membrane layers along the tank length to produce a strong resonance effect. Another reason

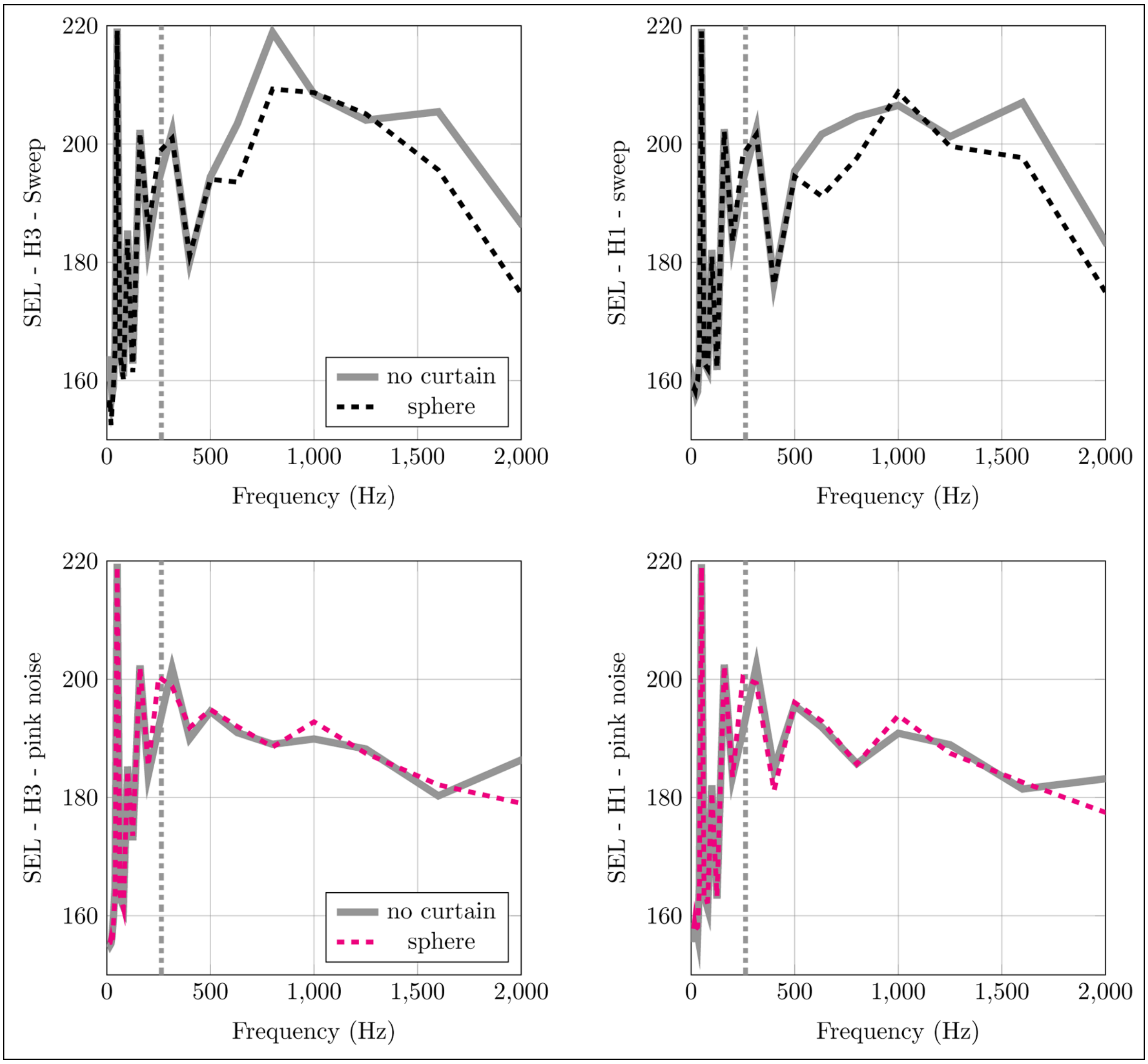

Figure 33. Insertion loss of a membrane containing ellipsoid bubbles. Measurements presented in (a and b) are related to the sweep signal at hydrophones H3 and H1, while measurements at (c and d) are related to the pink noise signal at hydrophones H3 and H1.

could be that the bubbles were made by two silicone parts, which could produce different resonant modes, in comparison to the continuous numerical bubbles. Additionally, the tank cross-section was only partially covered, allowing wave propagation through uncovered areas. Combined with reflections from the tank walls, this may have impacted the performance assessment. Therefore, improvements to the experimental setup are strongly recommended and will be outlined in the following section.

Recommendations for future steps

Different bubble designs with the same volume showed enhanced acoustic properties, paving the way for further exploration through optimization and machine learning. Additionally, the encapsulating membranes significantly influenced bubble resonance. This can be tuned passively by varying membrane thickness or materials, or actively using smart materials – for instance, leveraging pressure and temperature changes with water depth to adjust acoustic behavior.

The numerical analyses in this report focus on the effective acoustic properties of single free and encapsulated bubbles. To better reflect real conditions, future numerical work could incorporate the effect of the two-part fabrication by modeling the seam between the silicone halves as a geometric or material discontinuity, potentially using a full 3D finite element model to capture asymmetric resonance modes. Extending the analysis to bubble groups is recommended, as group resonance behavior differs from that of single bubbles (Jerez Boudesseul and Van't Wout, 2023), potentially affecting effective properties and the target attenuation

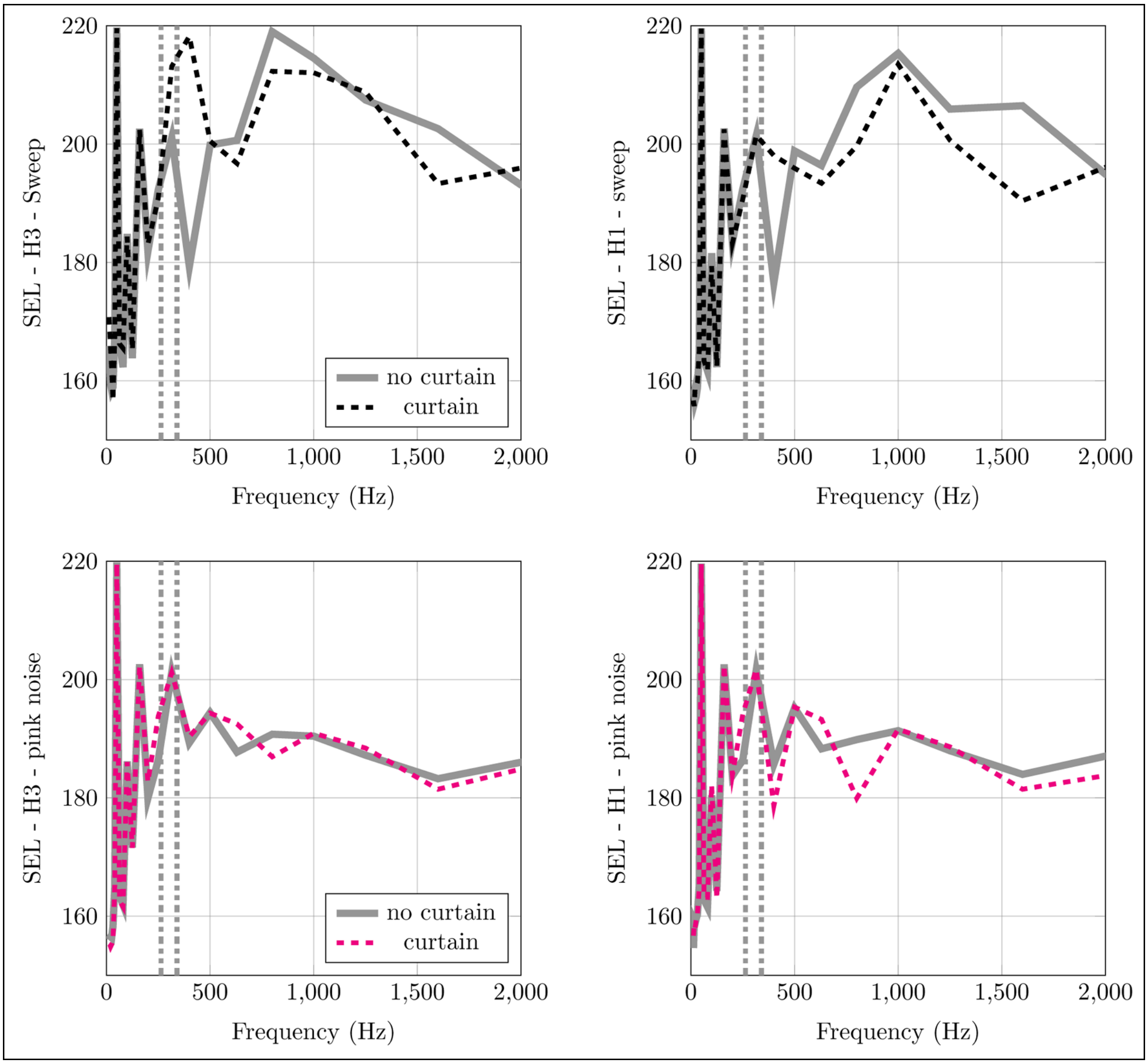

Figure 34. Insertion loss of a curtain containing all membranes and long balloons. Measurements presented in (a and b) are related to the sweep signal at hydrophones H3 and H1, while measurements at (c and d) are related to the pink noise signal at hydrophones H3 and H1.

range. Further investigation is also needed to determine the required bubble quantity to achieve specific sound reduction levels, which can be explored through both acoustic and vibroacoustic models.

The parametric design space explored in this study (bubble shape, membrane thickness, material stiffness) is well suited for data-driven optimization. Machine learning or surrogate modeling approaches could identify optimal cavity geometries that maximize attenuation bandwidth while minimizing material usage, leveraging the acoustic property trends established in Section "Numerical approach of effective acoustic parameters."

In terms of the experimental validation of the meta-curtain principle, some improvements on prototyping, experimental setup, and analysis are recommended. The adopted manufacturing strategy proved practical for producing encapsulated bubbles, though improvements are possible. Rather than gluing two separate membranes, injecting air into a single mold with an open cavity could yield more continuous, uniform bubbles that better match numerical models. This approach, however, would require more precise machinery to ensure consistent membrane thickness. Optimizing membrane geometry to embed more bubbles while maintaining structural integrity is also worth exploring. Additionally, alternative silicone materials could be investigated to enhance tunability of the bubbles' acoustic properties.

For offshore deployment, the silicone encapsulating membranes must withstand hydrostatic pressure, marine biofouling, UV degradation, and repeated dynamic loading from wave and current action. Ecoflex 00-35 silicone, used in the prototypes, exhibits high

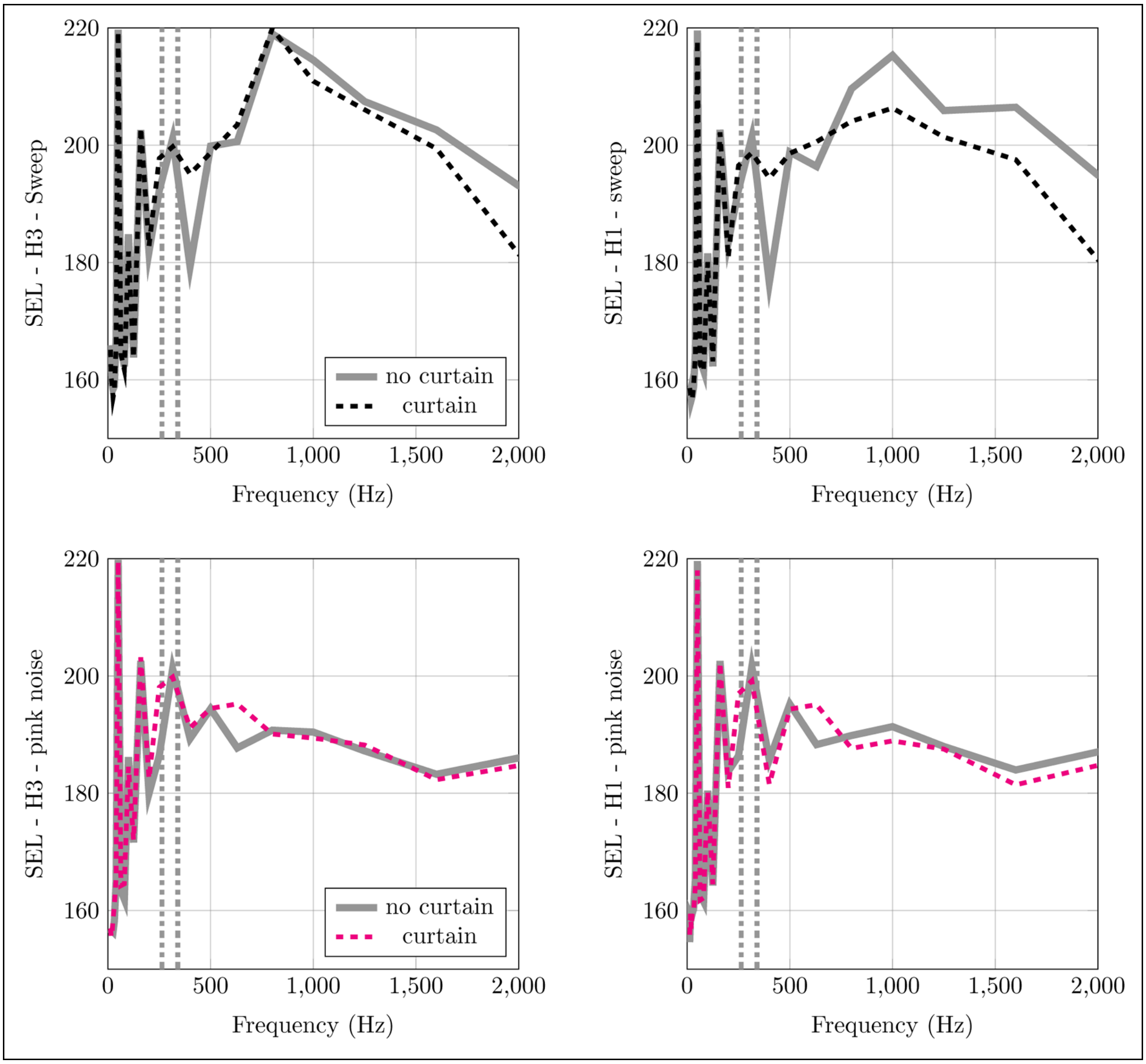

Figure 35. Insertion loss of a curtain containing only membranes. Measurements presented in (a and b) are related to the sweep signal at hydrophones H3 and H1, while measurements at (c and d) are related to the pink noise signal at hydrophones H3 and H1.

elongation at break and demonstrated adequate tear resistance during demolding and tank testing. For long-term deployment, alternative silicone formulations with enhanced UV resistance and antifouling properties should be evaluated. The flexibility of the encapsulation approach also enables passive tuning of bubble resonance with depth, as hydrostatic pressure compresses the air volume and shifts the resonance frequency, or active tuning through smart materials responding to pressure and temperature changes.

Measurements collected in closed tanks are affected by wave reflections induced by the tank walls, which introduce noise, increasing the complexity of analyzing the data, especially for the evaluation of sound measured for all hydrophones at the same test – the results presented in insertion loss diagrams are more clear. Thus, it is highly recommended that the tank walls should be covered by foam layers or that the measurements should be performed in offshore condition.

The observed attenuation is attributable to the bubble resonance mechanism rather than the membrane barrier alone. A plain silicone membrane without air cavities would present an acoustic impedance close to water, yielding minimal reflection and negligible attenuation. The engineered air cavities create a dramatic impedance contrast near the resonance frequency, as evidenced by the effective property transitions in Figures 9 and 11. A dedicated comparison experiment using a plain silicone membrane of identical dimensions is recommended for the next test campaign to rigorously isolate the resonance contribution from any residual barrier effect.

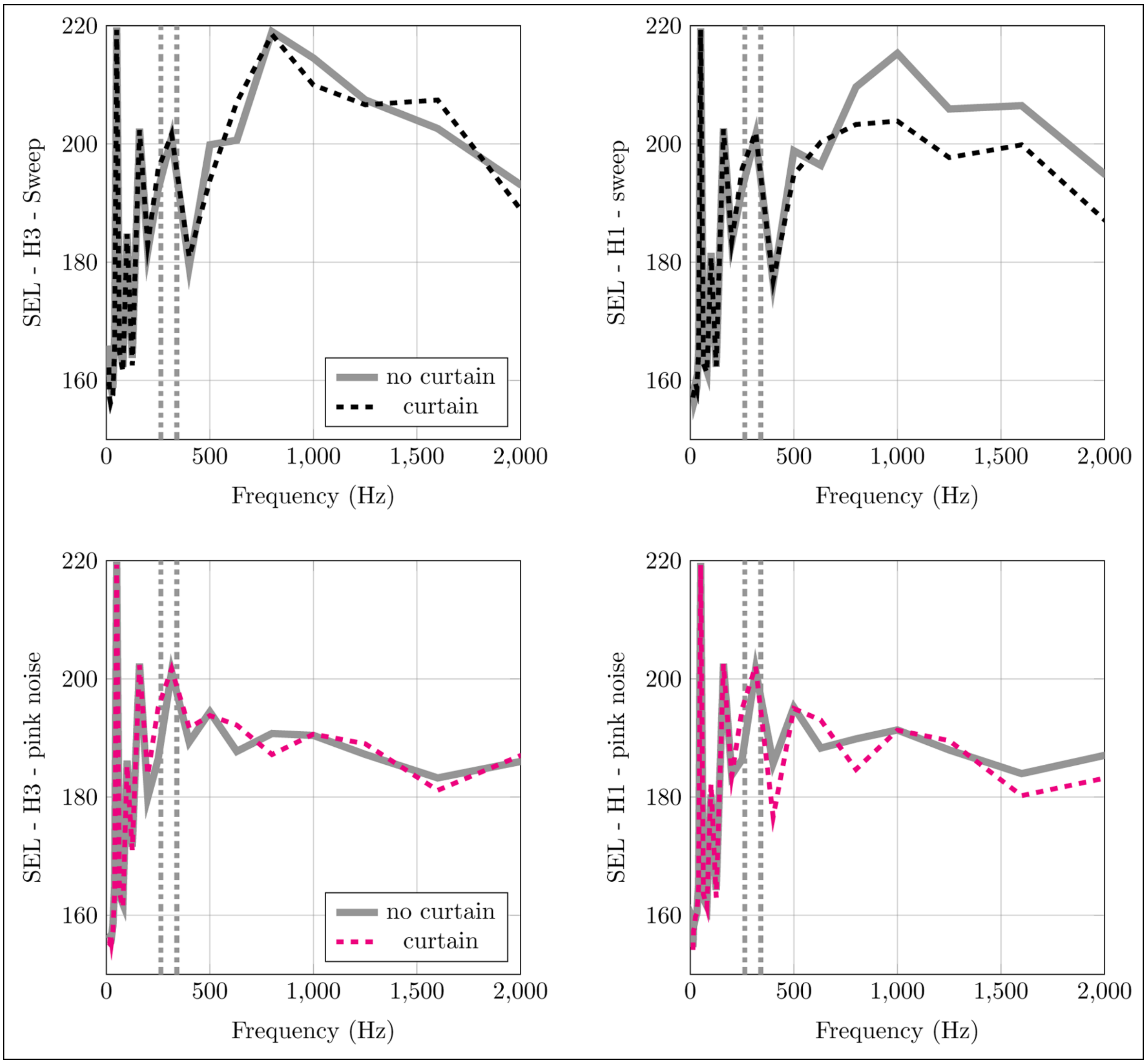

Figure 36. Insertion loss of a curtain containing all membranes, long balloons, and foam. Measurements presented in (a and b) are related to the sweep signal at hydrophones H3 and H1, while measurements at (c and d) are related to the pink noise signal at hydrophones H3 and H1.

A key challenge in the curtain prototype was assembling the bubbly membranes into a frame and positioning the structure underwater. Vertical stiff beams were used to prevent floating, but space limitations in the tank made placement difficult. Additionally, the rigid structure added weight, complicating deployment and increasing wave reflections, which introduced signal noise. Therefore, it is essential to develop lightweight, flexible frames that are strong enough to support the membranes and withstand wave currents, while enabling easier deployment. When designing the flexible frame for assembling bubbly membranes, defining the deployment mechanism is crucial. Literature identifies deployable structures with varied stiffness, classified as rigid, flexible, or rigid-flexible (Zhang et al., 2021. Accordingly, the meta-curtain could use either fully flexible structures – where both the frame and membranes are flexible – or a hybrid design combining a stiff frame with flexible bubbly membranes.

Acknowledgement

The authors would like to thank Delft University of Technology for enabling this research as a project awarded by the faculty of Mechanical Engineering.

ORCID iDs

Ana Carolina Azevedo Vasconcelos https://orcid.org/0000-0001-7624-8449
Jovana Jovanova https://orcid.org/0000-0001-8347-6386

Funding

The authors disclosed receipt of the following financial support for the research, authorship, and/or publication of this article: This research was funded through a grant of the Faculty of Mechanical Engineering at Delft University of Technology.

Declaration of conflicting interests

The authors declared no potential conflicts of interest with respect to the research, authorship, and/or publication of this article.

Data availability statement

Data sharing not applicable to this article as no datasets were generated or analyzed during the current study.

References

Beelen S, Nijhof M, de Jong C, et al. (2025) Bubble curtains for noise mitigation: One vs two. *Journal of the Acoustical Society of America* 157(2): 1336–1355.

Church CC (1995) The effects of an elastic solid surface layer on the radial pulsations of gas bubbles. *Journal of the Acoustical Society of America* 97(3): 1510–1521.

Commander KW and Prosperetti A (1989) Linear pressure waves in bubbly liquids: Comparison between theory and experiments. *Journal of the Acoustical Society of America* 85(2): 732–746.

Dahl PH, de Jong CA and Popper AN (2015) The underwater sound field from impact pile driving and its potential effects on marine life. *Acoustics Today* 11(2): 18–25.

Gao Y, Ma J and Ding Y (2021) Numerical simulation on the noise reduction of underwater pile-driving using a bubble curtain. *Journal of Physics Conference Series*1865: 032027.

Henríquez VC, García-Chocano VM and Sánchez-Dehesa J (2017) Viscothermal losses in double-negative acoustic metamaterials. *Physical Review Applied* 8(1): 014029.

IQIP (2024) Iqip's hydraulic impact hammer. Available at: https://iqip.com/products/pile-driving-equipment/hydrohammer/ (accessed 20 August 2024).

Jerez Boudesseul R and Van't Wout E (2023) Modeling frequency shifts of collective bubble resonances with the boundary element method. *Journal of the Acoustical Society of America* 153(3): 1898–1911.

Lippert S, Nijhof M, Lippert T, et al. (2016) Compile—a generic benchmark case for predictions of marine pile-driving noise. *IEEE Journal of Oceanic Engineering* 41(4): 1061–1071.

Ma Y and Yang J (2023) Earth pressure distribution on laterally loaded offshore monopiles. *Ocean Engineering* 273: 113954.

Murphy G, Igoe D, Doherty P, et al. (2018) 3d fem approach for laterally loaded monopile design. *Computers and Geotechnics* 100: 76–83.

Reinhall PG and Dahl PH (2011) Underwater mach wave radiation from impact pile driving: Theory and observation. *Journal of the Acoustical Society of America* 130(3): 1209–1216.

Solé M, Sigray P, Lenoir M, et al. (2017) Offshore exposure experiments on cuttlefish indicate received sound pressure and particle motion levels associated with acoustic trauma. *Scientific Reports* 7(1): 1–13.

Tsouvalas A (2020) Underwater noise emission due to offshore pile installation: A review. *Energies* 13(12): 3037.

Wang H, Wang LZ, Hong Y, et al. (2020) Quantifying the influence of pile diameter on the load transfer curves of laterally loaded monopile in sand. *Applied Ocean Research* 101: 102196.

Wang Z, Zhou W, Shu T, et al. (2022) Modelling of low-frequency acoustic wave propagation in dilute gas-bubbly liquids. *International Journal of Mechanical Sciences* 216: 106979.

WindEurope (2022) *Wind Energy in Europe: 2021 Statistics and the Outlook for 2022–2026*. WindEurope.

WindEurope (2023) Wind energy in Europe: 2023 statistics and the outlook for 2024-2030. Available at: https://windeurope.org/intelligence-platform/product/wind-energy-in-europe-2023-statistics-and-the-outlook-for-2024-2030/ (accessed 15 August 2024).

Zhang X, Nie R, Chen Y, et al. (2021) Deployable structures: Structural design and static/dynamic analysis. *Journal of Elasticity* 146(2): 199–235.